Subfilter-scale transport model for hybrid RANS/LES simulations applied to a complex bounded flow

Bruno Chaouat*
ONERA , 92322 Châtillon, France

Abstract

The partially integrated transport modeling (PITM) method viewed as a continuous approach of hybrid RANS/LES with seamless coupling is first recalled. In the present work, the subfilter stress model derived from the PITM method is considered and developed in a general formulation valid for free flows as well as bounded flows. Numerical simulations of the well known fully turbulent channel flows are first performed on coarse and medium grids for assessing the subfilter model and for studying the sharing out of the energy when the filter width is changed. The practical flow over a 2D periodic hills is then simulated on coarse and medium grids for illustrating the performances of the subfilter stress model. As a result, it is found that the subfilter stress model reproduces fairly well this complex flow governed by interacting turbulence mechanisms associated with separation, recirculation, reattachment, acceleration and wall effects. Overall, it provides velocity and turbulent stresses in good agreement with the reference data for both grids. The effects of the grid refinement are also investigated in detail. The solution trajectories projected onto the plane formed by the second and third invariants allow to analyze the realizability of the turbulent stresses and to assess the flow anisotropy. Moreover, the simulation using the subfilter stress model reveals the detail of the instantaneous flow structures. For comparison purposes, the channel flow over 2D hills is also predicted using a statistical Reynolds stress model (RSM) developed in RANS methodology. In contrast to the subfilter stress model used in LES methodology, it appears that the RSM model provides inaccurate results, in spite of being one of the most advanced RANS model. This failure seems to be attributed to the inability of RANS models to capture the large-scale dynamics in the separated shear layer.

1 Introduction

The mathematical turbulence modeling methods such as Reynolds Averaged Navier-Stokes (RANS) or Large Eddy Simulations (LES) methods [1] have been proposed independently from each other

*Senior Scientist, Department of Computational Fluid Dynamics. E-mail address: Bruno.Chaouat@onera.fr
This article was chosen from Selected Proceedings of the Sixth International Symposium on Turbulence and Shear Flow Phenomena (Seoul, Korea, 22-24 June 2009)

for simulating turbulent flows. Generally, advanced RANS models such as Reynolds Stress Models (RSM) [2] appear well suited for tackling engineering flows encountered in aeronautical or space applications [3, 4, 5, 6] whereas subgrid-scale models used in LES such as the dynamic model [7] or the structure model [8] are rather considered for simulating academic flows with emphasis on fundamental aspects and structural aspects. Although these methods are very useful, each of them has its own specific field of application. If statistical RANS models can reproduce unsteady flows governed by low frequencies, as for instance in applications to space launchers or solid rocket motors where vortex shedding phenomena play an important role [9], they are generally not well suited for simulating unsteady flows subjected to a large range of frequencies that can interact with the turbulence time scales. On the other hand, large eddy simulations initially devoted to the study of atmospheric flows [10] and fundamental flows are not accurate for simulating engineering flows when they are performed on coarse grids. The main reason arises from the location of the cutoff wave number which is placed in this case before the inertial range implying that a large part of subgrid energy is modeled despite the fact that the modeling uses simple closure only valid for fine grained turbulence. As mentioned by Spalart [11], it will not be possible in a near future to simulate industrial applications requiring large computational domains like for instance an entire aircraft, even with the rapid increase of super-computer power. The computational cost of such flow simulations still remains not affordable. For these reasons, hybrid RANS/LES methods capable of reproducing a RANS-type behavior in the vicinity of a solid boundary and an LES-type behavior far away from the wall boundary have been developed in the last decade [12, 13, 14]. Statistical and filtered equations can be written formally in the same form providing a convenient framework [7]. They differ by the turbulence models or parametrization needed to close the equations that allows the construction of composite methods. According to the literature, [6, 15] hybrid methods can be classified into two categories, zonal and non-zonal methods. RANS/LES zonal methods rely on two different models, a RANS model and a subgrid-scale model, which are applied in different domains separated by a sharp or dynamic interface [16, 17, 18]. Noticeably, the main shortcoming of these methods lies in the connection interface between the RANS and LES regions. The interface being empirically set inside the computational domain, the turbulence closure changes from one model to another one without continuity when crossing the interface. An internal forcing produced by artificial instantaneous random fluctuations is then necessary for restoring continuity at the crossflow between these domains in aiming to obtain correct velocity and stress profiles in the boundary layer [19, 20, 21]. The non-zonal methods assume that the governing set of equations is smoothly transitioning from a RANS behavior to an LES behavior, based on criteria updated during the computation. Among non-zonal methods, one can notice for instance blending turbulence models using a weighted sum of a RANS model and LES model by means of a blending factor [22]. But the terminology employed for classifying hybrid RANS/LES methods among zonal and non-zonal methods may be ambiguous since both use different models in different zones. Other authors [12] prefer to identify segregated modeling as a form of zonal methods and unified modeling corresponding to the counterpart to segregated modeling as non-zonal methods. Among these hybrid RANS/LES methods, the Detached Eddy Simulation (DES) [23, 11] where the model is switching from a RANS behavior to an LES behavior, depending on a criteria based on the turbulent length-scale, is one of the most popular models. However, although of practical use for aeronautical applications, DES is very sensitive to the interface position between the RANS

and LES regions and is also dependent on the grid-size. In particular, the gray area where the model varies from URANS to LES may be problematic unless the separation is abrupt and fixed by the geometry [11]. Note that a new version of the detached-simulation, referred to as DDES, for Delayed DES, resistant to ambiguous grid density, has been developed recently in this framework [24]. Usually, hybrid RANS/LES methods are inspired by RANS modeling that constitutes a convenient framework [25]. But other models can be devised by different routes rather than starting from existing RANS models. One can mention for instance the RG VLES model [26] relying upon renormalization group (RG) calculations [27]. The hybrid model proposed by Delanghe *et al.* [26] founded on RG modeling is a one-equation model based on the dissipation-rate equation unlike most one-equation model that are using the turbulent energy equation.

Recently, the Partially Integrated Transport Modeling (PITM) method has been developed by Chaouat and Schiestel [28] and by Schiestel and Dejoan [29] to overcome the difficulties raised by standard RANS/LES methods. This present PITM method gains major interest on the fundamental point of view because it allows some unifying formalism that conciliates both RANS and LES approaches [30]. This method is based on the spectral Fourier transform of the dynamic equation of the two-point fluctuating velocity correlations with an extension to the case of nonhomogeneous turbulence. The resulting equation describes the evolution of the spectral velocity correlation tensor in wave vector space [28, 30]. Then, partial integrations of the spectral equation give rise to subfilter turbulence models. This method is general and can be applied to almost all statistical models to derive their hybrid LES counterparts corresponding to subfilter models that can be used for performing continuous hybrid non-zonal RANS/LES simulations with seamless coupling on relatively coarse grids. Among these subfilter models derived by the PITM method, one can mention for instance subfilter viscosity models [29, 31] and subfilter stress models [28, 32, 33, 34] transposed from $k-\epsilon$, $k-\epsilon-\zeta$ models and Reynolds stress models, respectively. Subfilter scale stress models [28, 32, 34] that discard the concept of turbulent viscosity are the most elaborate models. Indeed, due to the presence of the subfilter scale pressure-strain correlation term in the transport equation, they provide a more realistic description of the flow anisotropy than eddy viscosity models. They are able to take into account precisely the turbulent processes of production, transfer, pressure redistribution effects, and dissipation. Subfilter models devised from the PITM method appreciably differ from standard non-zonal hybrid RANS/LES models based on RANS and LES models empirically matched by blending functions, because they are based on a continuous formulation. As a result, the PITM solution evolving in time and space is then governed by a dynamical parameter η_c involving the ratio of the turbulent length-scale to the grid-size. The turbulent quantities are calculated as the sum of the subfilter and resolved contributions. Note that the PANS method [35] also appears in this line of thought, and the final equations have great similarities with the PITM equations, despite a completely different argumentation based on practical considerations. The PANS method however imposes an arbitrary fixed ratio for the subgrid energy to the total energy. This method has been applied to devise only subgrid viscosity models.

The paper first presents briefly the PITM method and describes numerical flow simulations using a subfilter stress model developed in a general formulation for free flows as well as bounded flows [32, 36]. The fully developed turbulent channel flow is first simulated on two different grids

for checking the grid independence of the solutions as well as the consistency of the subfilter stress model when the filter width is changed. Then, the periodic flow over a 2D hill is simulated on coarse and medium grids by using both the subfilter stress model and the statistical RSM model for comparison purposes. The effects of the grid refinement are also investigated in detail. This test case of the separated flow in a channel with streamwise periodic constrictions is of central interest because of the turbulence mechanisms associated with separation, recirculation, reattachment, acceleration and wall flow effects that are difficult to accurately predict. This part constitutes the main issue of the present work.

2 The filtering process and transport equation subfilter model

2.1 The governing equations

Turbulent flow of a viscous incompressible fluid is considered. In large eddy simulations, the flow variable ϕ is decomposed into a large scale (or resolved) part $\bar{\phi}$ and a subfilter-scale fluctuating (or modeled) part ϕ'. The large scale component is defined by the filter function G_Δ as

$$\bar{\Phi}(\boldsymbol{x}) = \iiint_{\mathcal{D}} G_\Delta(\boldsymbol{x}, \boldsymbol{x'})\, \Phi(\boldsymbol{x'})\, d^3\boldsymbol{x'} \tag{1}$$

where Δ is the filter width. Applying the filtering operation to the instantaneous Navier-Stokes momentum equation yields the filtered momentum equation

$$\frac{\partial \bar{u}_i}{\partial t} + \frac{\partial}{\partial x_j}\left(\bar{u}_i \bar{u}_j\right) = -\frac{1}{\rho}\frac{\partial \bar{p}}{\partial x_i} + \nu \frac{\partial^2 \bar{u}_i}{\partial x_j \partial x_j} - \frac{\partial (\tau_{ij})_{sfs}}{\partial x_j} \tag{2}$$

where u_i, p, $(\tau_{ij})_{sfs}$, are the velocity vector, the pressure, and the subfilter-scale stress tensor, respectively. The subfilter-scale tensor $(\tau_{ij})_{sfs}$ is defined by the mathematical relation

$$(\tau_{ij})_{sfs} = \overline{u_i u_j} - \bar{u}_i \bar{u}_j \tag{3}$$

The presence of the turbulent contribution $(\tau_{ij})_{sfs}$ in equation (2) indicates the effect of the subfilter scales on the resolved field. The resolved scale tensor is defined by the relation

$$(\tau_{ij})_{les} = \bar{u}_i \bar{u}_j - \langle u_i \rangle \langle u_j \rangle \tag{4}$$

where $\langle . \rangle$ denotes the statistical average. So that, the Reynolds stress tensor τ_{ij} including the small and large scale fluctuating velocities is computed as the sum of the subfilter and resolved stresses

$$\tau_{ij} = \langle (\tau_{ij})_{sfs} \rangle + \langle (\tau_{ij})_{les} \rangle \tag{5}$$

whereas the statistical turbulent kinetic energy is obtained as the half-trace of the tensor τ_{ij} (5) leading to

$$k = \langle k_{sfs} \rangle + \langle k_{les} \rangle \tag{6}$$

2.2 The subfilter stress model

The subfilter stress modeling finds its physical foundation in the spectral space by considering the Fourier transform of the two-point fluctuating velocity correlation equations in homogeneous turbulence [30, 37]. The extension to non-homogeneous turbulence is developed within the framework of the tangent homogeneous space [30]. Note that a formalism based on temporal filtering has been also proposed recently to handle non-homogeneous flows leading to a variant of the PITM method using temporal filters and called Temporal Partial Integrated Transport Modeling (TPITM) method [38, 34]. From a physical point of view, it is assumed in the present LES framework that the interaction mechanisms of the subfilter-scales with the resolved scales of the turbulence are of the same nature than the interaction mechanisms involving all the fluctuating scales with the mean flow prevailing in RANS models, allowing transposition of closure hypotheses from RANS to LES. This hypothesis is so natural that it was already used in the pioneering work of Deardorff [39]. As a result, the subfilter model based on the transport equations for the subfilter-scale stresses $(\tau_{ij})_{sfs}$ and the subfilter dissipation rate ϵ_{sfs} look formally like the corresponding RANS/RSM model but the coefficients used in the model are no longer constants. They are now some functions of the dimensionless parameter η_c involving the cutoff wave number κ_c and the turbulent length scale L_e built using the total turbulent kinetic energy $k = \langle k_{sfs} \rangle + \langle k_{les} \rangle$, the total dissipation rate $\epsilon = \langle \epsilon_{sfs} \rangle + \langle \epsilon^{<} \rangle$ composed of the subfilter dissipation rate ϵ_{sfs} and the resolved macro-scale dissipation rate $\epsilon^{<}$

$$\eta_c = \kappa_c L_e = \frac{\pi \, k^{3/2}}{(\Delta_1 \Delta_2 \Delta_3)^{1/3} \, \epsilon} \tag{7}$$

The main feature of the PITM method is that the subfilter stress model varies now continuously with respect to the ratio of the turbulent length-scale to the grid-size L_e/Δ. For the limiting condition when the parameter η_c goes to zero, the subfilter stress model behaves like a RANS/RSM model whereas when η_c goes to infinity, the computation switches to DNS or under resolved DNS if the grid-size is not refined enough because the energy cannot be maintained. In regard with academic LES simulations, which require that the spectral cutoff must be located within the inertial range, the present subfilter stress model allows to perform flow simulations on relatively coarse grids since the cutoff wavenumber can be located almost anywhere inside the spectrum. By using the material derivative operator $D/Dt = \partial/\partial t + \bar{u}_k \partial/\partial x_k$, the transport equation of the subfilter stress tensor can be written in the simple compact form as

$$\frac{D(\tau_{ij})_{sfs}}{Dt} = P_{ij} + \Psi_{ij} + J_{ij} - (\epsilon_{ij})_{sfs} \tag{8}$$

where the terms appearing in the right-hand side of this equation are identified as production, redistribution, diffusion and dissipation, successively. The production term P_{ij} is produced by the interaction between the subfilter stress and the filtered gradient velocity

$$P_{ij} = -(\tau_{ik})_{sfs} \frac{\partial \bar{u}_j}{\partial x_k} - (\tau_{jk})_{sfs} \frac{\partial \bar{u}_i}{\partial x_k} \tag{9}$$

The redistribution, diffusion and dissipation terms need to be modeled. Like in RANS modeling, the redistribution term Ψ_{ij} can be decomposed into a slow part Ψ^1_{ij}, a rapid part Ψ^2_{ij} and a wall

reflexion term Ψ^3_{ij}. The slow term Ψ^1_{ij} characterizes the return to isotropy due to the action of turbulence on itself whereas the rapid term Ψ^2_{ij} describes the return to isotropy by action of the filtered velocity gradient. The wall reflexion term Ψ^3_{ij} accounts for the wall effects caused by the reflexion of the pressure fluctuation from rigid walls. The term Ψ^1_{ij} is modeled assuming that the usual statistical Reynolds stress models must be recovered in the limit of vanishing cutoff wave number κ_c and considering also that the small scales return more rapidly to isotropy than the large scales before cascading into smaller scales by non-linear interactions

$$\Psi^1_{ij} = -c_{sfs_1}\frac{\epsilon_{sfs}}{k_{sfs}}\left((\tau_{ij})_{sfs} - \frac{2}{3}k_{sfs}\,\delta_{ij}\right) \tag{10}$$

where c_{sfs_1} is an increasing function of the parameter η_c. This function is empirically proposed in the following form

$$c_{sfs_1}(\eta_c) = c_1\,\frac{1+\alpha_{\eta 1}\,\eta_c^2}{1+\alpha_{\eta 2}\,\eta_c^2} \tag{11}$$

where in this relation, c_1 is the usual Rotta constant used in statistical modeling and $\alpha_{\eta 1}$, $\alpha_{\eta 2}$ are constant coefficients. The second term Ψ^2_{ij} is modeled by

$$\Psi^2_{ij} = -c_2\left(P_{ij} - \frac{1}{3}P_{mm}\,\delta_{ij}\right) \tag{12}$$

where the coefficient c_2 remains the same than in statistical modeling. The wall reflexion term is modeled by [40]

$$\begin{aligned}\Psi^3_{ij} &= c_{1w}\frac{\epsilon_{sfs}}{k_{sfs}}\left((\tau_{kl})_{sfs}n_k n_l\delta_{ij} - \tfrac{3}{2}(\tau_{ki})_{sfs}n_k n_j - \tfrac{3}{2}(\tau_{kj})_{sfs}n_k n_i\right)f_w \\ &+ c_{2w}\left(\Psi^2_{kl}n_k n_l\delta_{ij} - \tfrac{3}{2}\Psi^2_{ik}n_k n_j - \tfrac{3}{2}\Psi^2_{jk}n_k n_i\right)f_w\end{aligned} \tag{13}$$

where in this expression, n_i is the unit vector perpendicular to the wall and f_w is a near wall damping function. The diffusion term J_{ij} appearing in equation (8) due to the fluctuating velocities and pressure together with the molecular diffusion, is modeled assuming a gradient law hypothesis

$$J_{ij} = \frac{\partial}{\partial x_k}\left(\nu\frac{\partial(\tau_{ij})_{sfs}}{\partial x_k} + c_s\frac{k_{sfs}}{\epsilon_{sfs}}(\tau_{kl})_{sfs}\frac{\partial(\tau_{ij})_{sfs}}{\partial x_l}\right) \tag{14}$$

where c_s is a numerical coefficient. Closure of equation (8) requires to model the subfilter tensorial dissipation rate $(\epsilon_{ij})_{sfs}$ which is approached by $(2/3)\epsilon\delta_{ij}$. The modeling of dissipation-rate ϵ_{sfs} is made in the present case by means of its transport equation. This allows to obtain an accurate estimate of the subfilter dissipation rate even in situation of non-equilibrium flows when the grid-size is no longer a good estimate of the characteristic turbulence length-scale [41]. As a result of the theory developed in the spectral space [30, 42], the fluctuating modeled transport equation for the subfilter-scale dissipation-rate ϵ_{sfs} reads

$$\frac{D\epsilon_{sfs}}{Dt} = c_{sfs\epsilon_1}\frac{\epsilon_{sfs}}{k_{sfs}}P - c_{sfs\epsilon_2}\frac{\epsilon^2_{sfs}}{k_{sfs}} + J_\epsilon \tag{15}$$

where $P = P_{mm}/2$. The coefficient $c_{sfs\epsilon_1}$ is constant whereas the coefficient $c_{sfs\epsilon_2}$ appearing in equation (15) is found to be a function of the ratio of the subfilter energy to the total energy $\langle k_{sfs} \rangle / k$ as follows [30]

$$c_{sfs\epsilon_2} = c_{\epsilon_1} + \frac{\langle k_{sfs} \rangle}{k} (c_{\epsilon_2} - c_{\epsilon_1}) \tag{16}$$

and where the coefficients c_{ϵ_1} and c_{ϵ_2} appearing in this equation denote the usual constants used in the statistical dissipation rate transport equation. The theory shows that the coefficients of the production term remain the same for both RANS and LES dissipation-rate equations $c_{sfs\epsilon_1} = c_{\epsilon_1} = 3/2$. One can notice that the method can be adapted when the reference RANS constant coefficient c_{ϵ_1} is not equal to 3/2, and the relation (16) is still valid. Equation (15) using the relation (16) constitutes the main feature of the PITM approach where only the part of the spectrum for $\kappa > \kappa_c$ is modeled. The ratio $\langle k_{sfs} \rangle / k$ appearing in equation (16) is evaluated by means of an accurate energy spectrum $E(\kappa)$ inspired from a Von Kármán like spectrum valid on the entire range of wavenumbers

$$E(\kappa) = \frac{\frac{2}{3}\beta_\eta L_e^3 \, k \, \kappa^2}{[1 + \beta_\eta (\kappa \, L_e)^3]^{11/9}} \tag{17}$$

where β_η is a constant coefficient, leading to the result [32]

$$\frac{\langle k_{sfs} \rangle}{k} = [1 + \beta_\eta (\kappa_c L_e)^3]^{-2/9} \tag{18}$$

So that $c_{sfs\epsilon_2}$ takes the analytical expression

$$c_{sfs\epsilon_2}(\eta_c) = c_{\epsilon_1} + \frac{c_{\epsilon_2} - c_{\epsilon_1}}{[1 + \beta_\eta \, \eta_c^3]^{2/9}} \tag{19}$$

However, one has to keep in mind that the computed energy spectrum shape is not universal and is locally evolving in time and space. In practice, the computed ratio value $\langle k_{sfs} \rangle / k$ provided by the LES simulation may slightly differ from the solution of equation (18). This usual situation occurs for flows that are out of spectral equilibrium. The ϵ equation then works in order to bring the calculated $\langle k_{sfs} \rangle / k$ value close to the analytical equilibrium value. The use of the Von Kármán spectrum allows to satisfy automatically the limiting condition when the subfilter energy approaches the total energy. Equation (19) indicates that the function $c_{sfs\epsilon_2}$ acts like a dynamical parameter which controls the spectral distribution of turbulence and verifies the limiting conditions $lim_{\ \eta_c \to 0} \ c_{sfs\epsilon_2}(\eta_c) = c_{\epsilon_2}$ and $lim_{\ \eta_c \to \infty} c_{sfs\epsilon_2}(\eta_c) = c_{\epsilon_1}$. At this step, it is of importance to note that equation (15) is related to the subfilter spectral interval $[\kappa_c, \infty[$ and that the source term involves the energy flux P through the cutoff which depends on the location of κ_c [28]. However, the value of the dissipation-rate itself is obviously physically independent of κ_c. When integrating the spectral energy equation in the $[\kappa_c, \infty[$ interval, one can find that the coefficient $c_{sfs\epsilon_2}$ is consequently dependent on κ_c so that the terms in balance appearing in equation (15) allows to recover a dissipation-rate value independent of κ_c. This is physically consistent, contrary to what was asserted in reference [26]. The theoretical value of the coefficient β_η appearing in equation (19) is obtained by the limiting condition of the Kolmogorov law at high wavenumbers $\lim_{\kappa \to \infty} E(\kappa) = C_K \epsilon^{2/3} \kappa^{-5/3}$ where C_K is the Kolmogorov constant leading to the theoretical value

$\beta_{\eta_{th}} = [2/(3C_K)]^{9/2}$. The diffusion term J_ϵ appearing on the right hand side of equation (15) is modeled assuming a well-known gradient law hypothesis

$$J_\epsilon = \frac{\partial}{\partial x_j}\left(\nu\frac{\partial \epsilon_{sfs}}{\partial x_j} + c_\epsilon \frac{k_{sfs}}{\epsilon_{sfs}}(\tau_{jm})_{sfs}\frac{\partial \epsilon_{sfs}}{\partial x_m}\right) \tag{20}$$

where c_ϵ is a constant coefficient. The present subfilter stress model formulation is extended to low Reynolds number flows using the functions listed in table 1 and the second and third subfilter-scale invariants defined by $A_2 = a_{ij}a_{ji}$, $A_3 = a_{ij}a_{jk}a_{ki}$, the flatness parameter $A = 1 - \frac{9}{8}(A_2 - A_3)$ where $a_{ij} = [(\tau_{ij})_{sfs} - \frac{2}{3}k_{sfs}\delta_{ij}]/k_{sfs}$. The numerical coefficients are the following : $\alpha_{\eta 1} = 1.3/400$, $\alpha_{\eta 2} = 1/400$, $c_s = 0.22$, $c_\epsilon = 0.18$, $c_{\epsilon_1} = 1.45$, $c_{\epsilon_2} = 1.9$.

Functions	Expressions
R_t	$k_{sfs}^2/(\nu\epsilon_{sfs})$
c_1	$1 + 2.58AA_2^{\frac{1}{4}}\left[1 - \exp(-(R_t/150)^2)\right]$
c_2	$0.6A^{\frac{1}{2}}$
c_{1w}	$-\frac{2}{3}c_1 + \frac{5}{3}$
c_{2w}	$\max(\frac{2}{3}c_2 - \frac{1}{6}, 0)/c_2$
f_w	$0.4k_{sfs}^{3/2}/(\epsilon_{sfs}x_n)$

Table 1: Functions used in the subfilter stress model.

2.3 Limiting behavior for the subfilter stress model

From a theoretical point of view, it is of interest to analyze the asymptotic behavior of the subfilter stress model when the cutoff location approaches the upper limit of the energy spectrum wavenumber interval. Considering a spectral equilibrium situation in the inertial zone governed by the Kolmogorov law, the theoretical ratio of the subfilter energy to the total energy takes the value $\langle k_{sgs}\rangle / k \approx (3C_K/2)\,\eta_c^{-2/3}$. In this case, it is a straightforward matter to show that the subfilter characteristic length scale goes to the filter width

$$\frac{\langle k_{sgs}\rangle^{3/2}}{\langle \epsilon_{sgs}\rangle} = \frac{\Delta}{\pi}\left(\frac{3C_K}{2}\right)^{3/2} \tag{21}$$

The subfilter stress model allows to compute the subfilter stress $(\tau_{ij})_{sfs}$ thanks to the transport equations (8) and (15) so that the concept of the turbulent viscosity is discarded. But it is still possible to define a tensorial viscosity given by $(\nu_{ij})_{sgs} = c_\nu(\langle k_{sgs}\rangle\,(\tau_{ij})_{sgs})/\epsilon_{sgs}$. For the sake of clarity, due to the fact that the small scales become isotropic at high Reynolds number, $\lim_{\eta_c\to\infty}\langle(\tau_{ij})_{sgs}\rangle = 2/3\,\langle k_{sgs}\rangle\,\delta_{ij}$, it is simpler to analyze the case of a scalar viscosity given by $\nu_{sgs} = c_\nu\,\langle k_{sgs}\rangle^2\,/\,\langle\epsilon_{sgs}\rangle$. Assuming a local equilibrium situation inside a very small slice in the far end of the energy spectrum, $\langle\epsilon_{sgs}\rangle = 2\nu_{sgs}\left\langle\bar{S}_{ij}\bar{S}_{ij}\right\rangle$ with $\bar{S}_{ij} = (\partial\bar{u}_i/\partial x_j + \partial\bar{u}_j/\partial x_i)/2$, it can be

shown for a two-equation model [32] that the limiting behavior for the subfilter viscosity ν_{sgs} is then given by

$$\nu_{sgs} = \frac{1}{\pi^2}\left(\frac{3C_K}{2}\right)^3 c_\nu^{3/2}\Delta^2\left[2\left\langle \bar{S}_{ij}\bar{S}_{ij}\right\rangle\right]^{1/2} \tag{22}$$

This expression shows that the subfilter model behaves like a Smagorinsky model. When performing flow simulations on refined grids using the PITM method, the computations which are sensitive to the grid-size through the parameter η_c defined in equation (7) progressively go to highly resolved LES.

3 Numerical method and conditions of computations

3.1 Numerical method

The numerical simulations are performed by using the research code developed by Chaouat [43] which is based on a finite volume technique. The governing equations of motion as well as the transport equations of the subfilter stresses and dissipation-rate are integrated in time by a Runge-Kutta scheme of fourth-order accuracy. The source terms of the turbulent equations are solved by an implicit scheme that improves the numerical stability and ensures the positivity of the normal stresses at each step of the computation. The convective fluxes at the interfaces resulting from the finite volume technique are computed by a numerical scheme of second-order and fourth-order accuracy in space which is based on a quasi-centered discretized formulation of the flow variables [44]. Previous simulations have shown that the numerical method is well appropriate for performing LES simulations [32]. It has been found also that the second order space accurate numerical scheme is sufficient for performing LES simulations. The decay of homogeneous isotropic turbulence referring to the well known experiment of Comte-Bellot and Corssin [45] has been fairly well reproduced as well as the decay of perturbed spectra with a peak or defect of energy, showing a qualitative agreement with EDQNM (eddy damped quasi-normal Markovian) spectral model predictions [46]. Several trial and error tests have been made for selecting appropriate values for the β_η coefficient. This coefficient β_η has been set to the value 0.0355 corresponding to a Kolmogorov constant $C_K = 1.4$ with the aim to obtain an appreciable part of the subfilter energy in comparison with the resolved energy. This value is calibrated once-for-all. Although more equations need to be solved at each time advancement, the CPU time consuming is reduced in regard with highly resolved LES because the simulations can be performed on very coarse grids. The simulations are worked out on the NEC-SX8 supercomputer and the parallelized code is running approximately at 30 GFLOPS in practice.

4 Fully turbulent channel flow

The test case of the fully developed turbulent channel flow is considered for analyzing the potentials of the subfilter stress model regarding its capacity to reproduce the flow anisotropy and wall flows. Different grids are generated with coarse and medium resolutions $16 \times 32 \times 64$ and $32 \times 64 \times 84$, respectively in the streamwise, spanwise and normal directions (x_1, x_2, x_3) for checking the grid

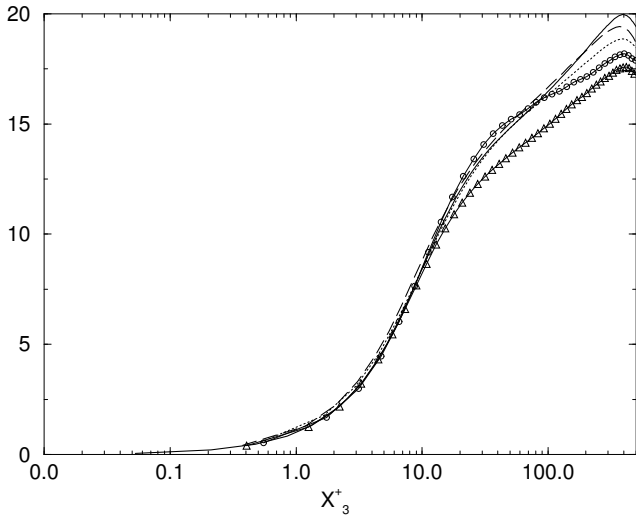

Figure 1: Mean velocity profile; $\langle u_1 \rangle / u_\tau$ PITM 1 ($16 \times 32 \times 64$) ...; PITM 2 ($32 \times 64 \times 84$) - -; SM 1 ($32 \times 64 \times 64$) Δ; SM 2 ($32 \times 64 \times 84$) $\circ$; DNS —; $R_\tau = 395$.

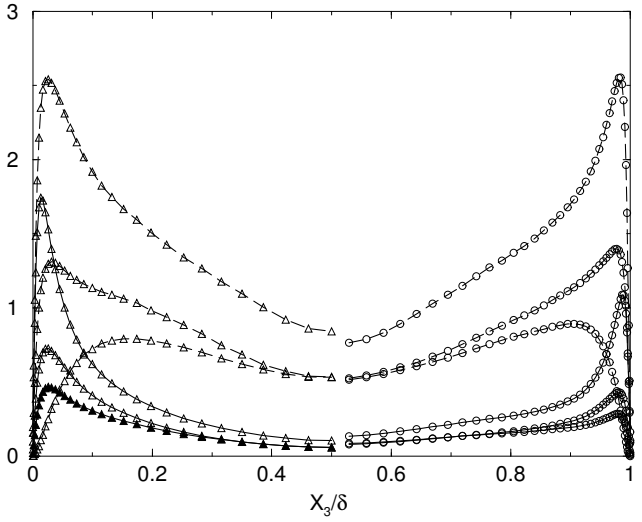

Figure 2: Subfilter stresses $\langle (\tau_{ii})_{sfs} \rangle^{1/2} / u_\tau$ and resolved stresses $\langle (\tau_{ii})_{les} \rangle^{1/2} / u_\tau$. Δ: PITM 1; $\circ$: PITM 2. i=1,2,3 from top. Subgrid energy —; Resolved energy - -

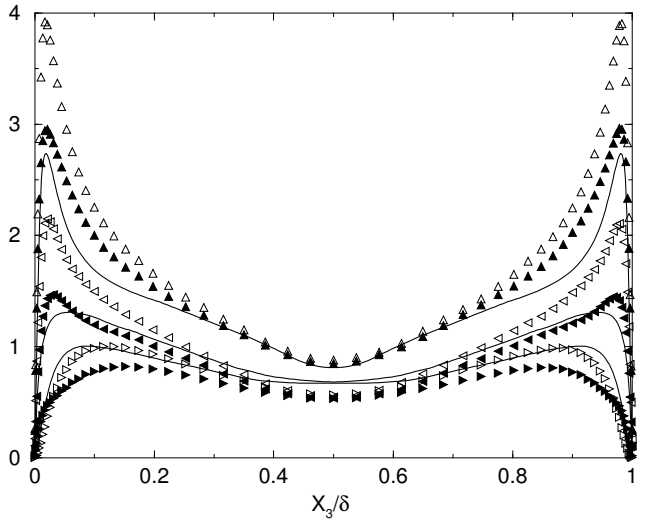

Figure 3: Turbulent Reynolds stresses $\tau_{ii}^{1/2}/u_\tau$. $(16 \times 32 \times 64)$. PITM : ▲: i=1; ◀: i=2; ▶: i=3; SM : △: i=1; ◁: i=2; ▷: i=3; DNS :—; $R_\tau = 395$.

independence of the solutions. The dimensions of the channel are $2\delta \times 2\delta \times \delta$. A minimal size of the box has been retained considering that these calculations are time consuming. But it has been checked in previous simulations [28] that the box size is sufficient for ensuring the vanishing of two-point correlation functions in the streamwise direction. In the normal direction to the wall, the grid points are distributed using non-uniform spacing with refinement near the wall whereas they are uniform in the two remaining directions, $\Delta_1^+ = 105.3$, $\Delta_2^+ = 50.9$ for case 1 and $\Delta_1^+ = 50.9$, $\Delta_2^+ = 25.1$ for case 2. The PITM results are compared with DNS [47] for a Reynolds number $R_\tau = 395$, based on the friction velocity u_τ and the channel half width $\delta/2$. For comparison purposes, numerical LES simulations using the Smagorinsky model in a version proposed by Lilly [48] are also performed on the coarse grid $16 \times 32 \times 64$. Figure 1 shows the profiles of the statistical mean velocity $\langle u_1 \rangle / u_\tau$ for both PITM and Smagorinsky simulations. The PITM profiles agree very well with DNS data whereas the Smagorinsky profiles strongly deviate from the DNS data in the logarithmic region. Figure 2 displays the evolutions of the subfilter and resolved stresses in the streamwise, spanwise and normal direction, respectively, for the coarse and medium grids. One can see that the subfilter scale stresses are indeed anisotropic in the vicinity of the walls and that the sharing out of the turbulence energies is governed by the grid size. Figure 3 describes the evolutions of the normalized total Reynolds stresses $\tau_{ii}^{1/2}/u_\tau = (\langle (\tau_{ii})_{sgs} \rangle + \langle (\tau_{ii})_{les} \rangle)^{1/2}/u_\tau$ (i=1,3) for the simulation performed on the coarse grid $16 \times 32 \times 64$. As a result, it appears that the stresses produced by the subfilter model agree well with the DNS data whereas the stresses computed by the Smagorinsky model highly overpredict the DNS data.

5 Channel flow with streamwise periodic constrictions

5.1 Computational framework

Numerical PITM simulations of the periodic flow over 2D hills are performed on a very coarse grid and on a medium grid by using the present subfilter stress model. For comparison purposes, RANS simulations using the Reynolds stress model (RSM) defined in reference [5, 43] are also undertaken on the coarse grid. This flow over periodic hills is considered because it constitutes a challenging test case which embodies turbulence mechanisms associated with separation, recirculation, reattachment, acceleration that are difficult to reproduce numerically. The flow is highly unsteady and governed by the separation and three dimensional wall effects. Initially, the hill configuration was proposed as a benchmark case at the 10^{th} joint "ERCOFTAC/IAHR/COST Workshop on Refined Turbulence Modeling "[49] for assessing the turbulence models ranging from RANS to LES. It has been found that RANS models performed badly this flow providing also disparate solutions. The simulations on coarse grids indicated a sensitive dependence of the mean reattachment location on the separation. Temmerman *et al.* [50] performed numerical simulations on coarse, medium and refined grids by using six subgrid-scale models including for instance the Wall-Adapting Local Eddy-Viscosity Model (WALE) and eight practices of approximating the near wall-region for identifying the sensitivity of the solutions to subgrid-scale modeling, grid density and wall treatments. Their simulations on coarse grids point out the importance of an adequate streamwise resolution of the flow in the separation zone. Saric *et al.* [51] performed detached eddy simulation on different grids showing acceptable results. The grid-resolutions were sufficiently fine for predicting accurately the separation point but the majority of the DES computations delayed the reattachment locations roughly at $x_1/h \approx 5$ although some differences were observed between these simulations [51]. As a result, the mean streamwise velocity profiles exhibited relatively good agreement with the reference data although some discrepancies were observed in the regions prior and after flow reattachment. Furthermore, the turbulent kinetic energy within the reattachment region was underpredicted and the near-wall peaks of the turbulent stresses were not accurately captured by these DES simulations. Breuer *et al.* [52] performed simulations on a coarse grid by using hybrid RANS/LES models. They mention encouraging results, similar or better than DES if considering a suitable interface criteria. Fröhlich *et al.* [53] and Breuer *et al.* [54] performed highly resolved simulations on refined grids by using the Dynamic Smagorinsky Model (DSM) with the aim of investigating the physics of this flow and also for providing a reference data base. More recently, Jakirlic *et al.* [31] performed continuous non-zonal hybrid RANS/LES simulations on a very coarse grid by using a subfilter energy model $k-\epsilon-\zeta-f$ derived from the PITM method. Promising results were obtained for the mean flow variables including the velocity, the shear stress and the turbulent energy. For the clarity of presentation, these simulations are summarized in table 2. In the present work, we perform numerical simulations of the constricted channel flow on the same coarse grid than those used in reference [31] and also on a medium grid for assessing the effects of the grid refinement, and we compare the results with the reference data provided by Breuer *et al.* [54].

The hills constricts the channel by about one third of its height and are spaced at a distance of about 9 hill heights. The Reynolds number, based on the hill height h and the bulk velocity

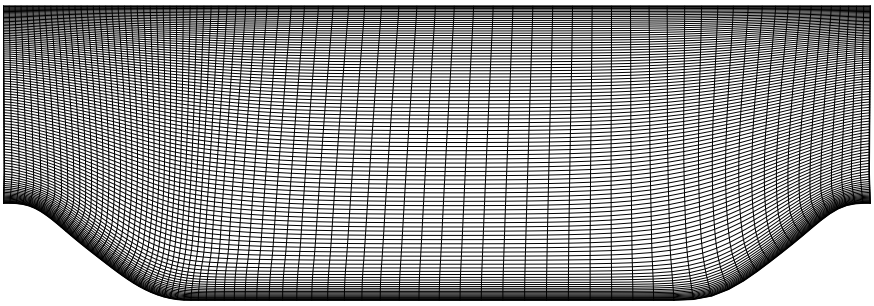

Figure 4: Cross-section of the curvilinear grid 80×100 of the contracted channel

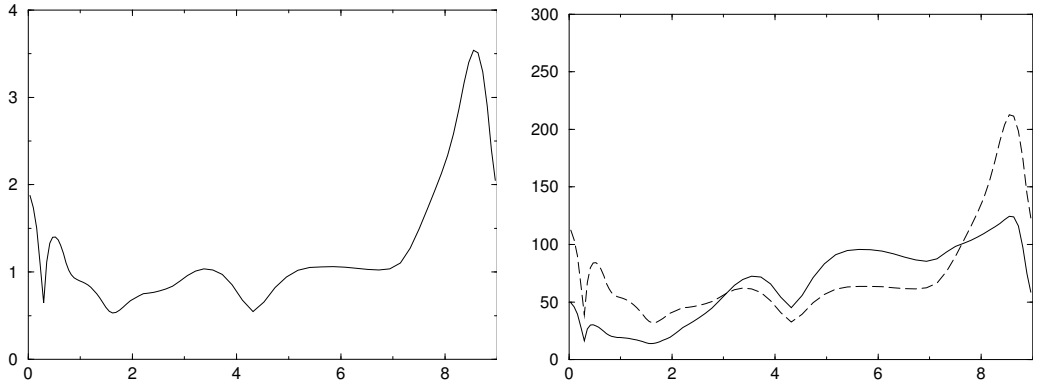

(a) x_1/h (b) x_1/h

Figure 5. Dimensionless grid spacings in wall units $\Delta^+ = \Delta u_\tau/\nu$ where u_τ is the friction velocity. (a) – normal direction Δ_3^+; (b) – streamwise direction Δ_1^+; - - spanwise direction Δ_2^+. PITM1 $(80 \times 30 \times 100)$.

Authors	Turbulence model	Grid points	$(x_1/h)_{sep}$	$(x_1/h)_{reat}$
Temmerman *et al.*, 2005[50]	WALE	7. 10^5	1.12	2.17
		10^6	0.38	3.45
		4.6 10^6	0.22	4.72
Saric *et al.*, 2005 [51]	DES	5. 10^5	0.214	4.957
		7. 10^5	0.214	5.012
		10^6	0.182	5.123
Fröhlich *et al.*, 2005 [53]	DSM	5. 10^6	0.20	4.56
Breuer *et al.*, 2008 [52]	Hybrid RANS/LES model (A)	10^6	0.254	4.751
Breuer *et al.*, 2009 [54]	DSM	13.1 10^6	0.190	4.694
Jakirlic *et al.*, 2009 [31]	PITM $k-\epsilon-\zeta-f$ model	2.5. 10^5	0.20	4.00
Chaouat, present CFD	RSM model	2.5 10^5	0.294	2.771
	PITM $(\tau_{ij})_{sfs}-\epsilon$ model	2.5 10^5	0.293	4.314
		10^6	0.279	4.366

Table 2: Simulations of flow over periodic hills including separation and reattachment locations.

U_b at the hill crest $Re = U_b h/\nu$ is about 10595. Different boundary conditions are applied in the computational domain. The simulated domain is periodic in the streamwise and spanwise directions. The streamwise periodic condition removes the need to specify the inflow condition allowing the assessment of the subfilter stress model without any contamination and potential sources of errors. No-slip and impermeability boundary conditions are used at the lower and upper walls. As usually, a mean pressure gradient term is included in the momentum equation for balancing the viscous friction at the walls but it is adjusted in time to reach the desired Reynolds number value at each instant. The statistics of the fluctuating velocity correlations is achieved in space in the spanwise homogeneous direction and in time using a recursive filter.

5.2 Computational grids

The exact dimensions of the computational domain are $L_1 = 9h$, $L_2 = 4.5h$ and $L_3 = 3.036h$, in the streamwise, spanwise and normal directions, respectively. As previously investigated in detail by Fröhlich *et al.* [53] by means of the two-point correlation function, the dimension in the spanwise direction is found to be sufficient for providing accurate results with an affordable computational cost. Numerical PITM simulations are performed on a coarse curvilinear grid $80 \times 30 \times 100$ ($\approx 1/4$ million grid points) and on a medium grid $160 \times 60 \times 100$ (≈ 1 million grid points) in the streamwise, spanwise and normal directions, (x_1, x_2, x_3). Figure 4 shows the cross-section of the curvilinear coarse grid. The grid has been refined in the lower and upper wall regions for accurately computing the boundary layers whereas it is coarser in the center of the channel. One can see also that the grids in the streamwise direction are more refined beyond the hill crest than in the mid-distance of the channel in order to accurately reproduce the flow separation caused by the hill geometry, and

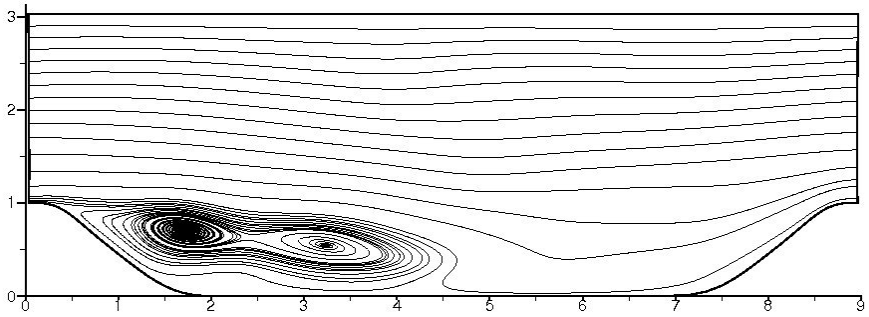

(a)

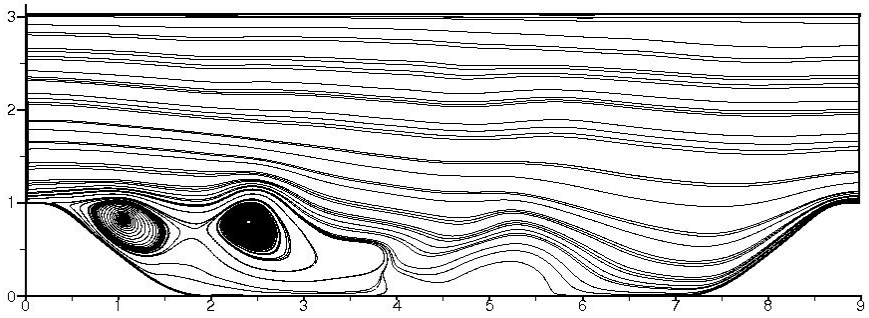

(b)

Figure 6. Streamlines of the instantaneous flowfield in the mid-plane of the channel at $x_2/h = 2$. (a) PITM1 simulation ($80 \times 30 \times 100$). (b) PITM2 simulation ($160 \times 60 \times 100$).

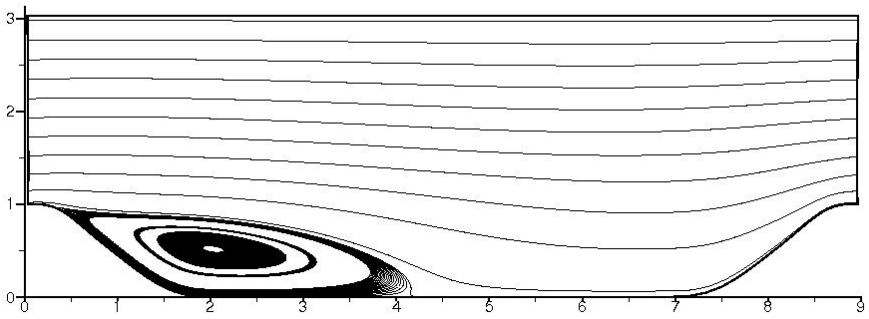

(a)

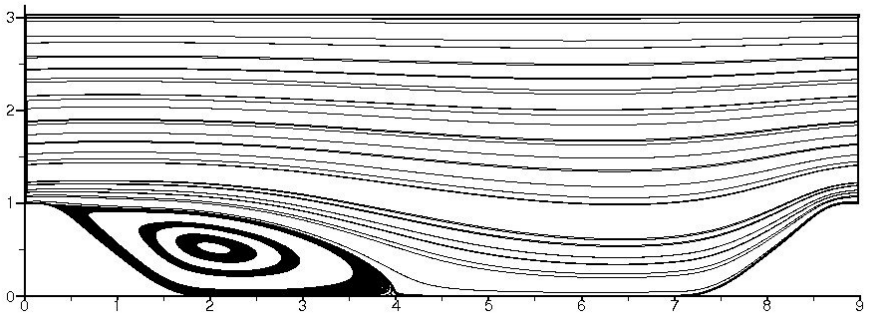

(b)

Figure 7. Streamlines of the average flowfield. (a) PITM1 simulation ($80 \times 30 \times 100$). (b) PITM2 simulation ($160 \times 60 \times 100$).

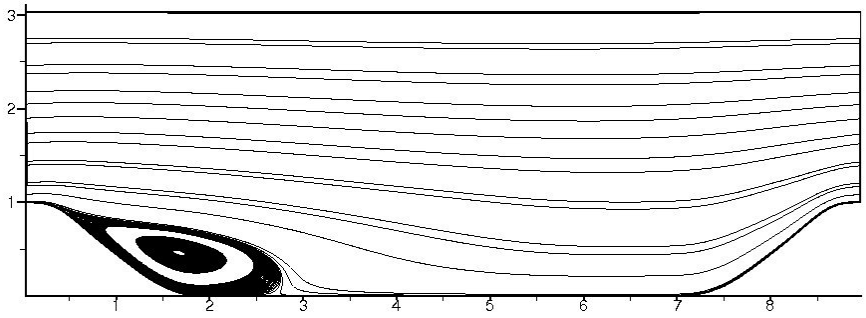

Figure 8: Streamlines of the flowfield. RSM computation ($80 \times 30 \times 100$).

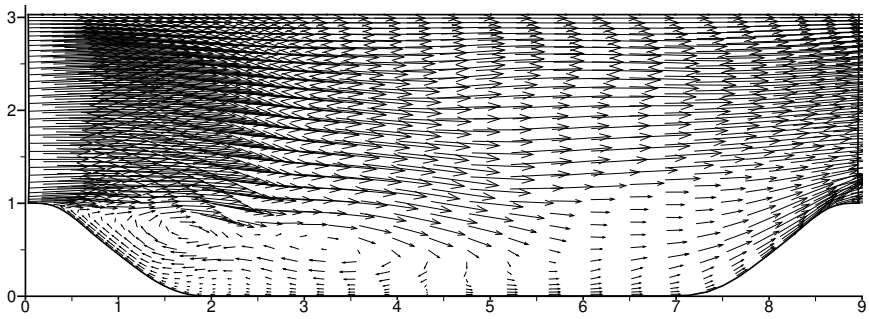

Figure 9: Vector plot of the instantaneous flow in the plane $x_2/h = 2$. An arrow is shown at each second grid point, horizontally, and at third grid point, vertically. PITM1 simulation ($80 \times 30 \times 100$).

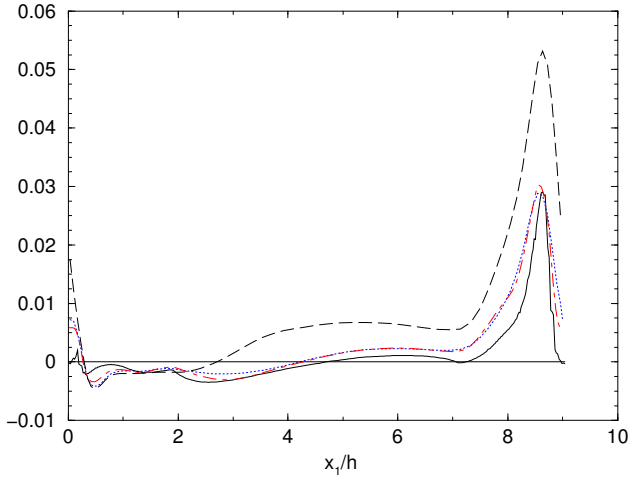

Figure 10: Friction coefficient $C_f = \tau_w/(0.5\rho U_b^2)$ along the lower wall LES (Breuer *et al.*, 2009) —; PITM1 ($80 \times 30 \times 100$) $\cdots$; PITM2 ($160 \times 60 \times 100$); -.-.-.; RSM - -.

to properly describe the flow recirculation as well as the reattachment of the boundary layer. This region beyond the hill constitutes the key region. Figure 5 displays the dimensionless grid spacings in wall unit $\Delta^+ = \Delta u_\tau/\nu$ in the streamwise, normal and spanwise directions where $u_\tau = \sqrt{\tau_w/\rho}$ denotes the shear stress velocity along the lower wall for the PITM1 simulation performed on the coarse grid. As usually, the grid spacing in the normal direction is computed by using the distance between the wall and the first grid point. A first sight of this figure indicates that the computed dimensionless distances Δ_3^+, Δ_1^+ and Δ_2^+ vary along the lower wall with respect to the streamwise distance, showing a decrease beyond the first hill crest followed by an increase in the windward slope of the second hill crest. The dimensionless distance Δ_3^+ in the normal direction to the lower wall is of the order of unity except in the windward region of the hill where Δ_3^+ approaches 3.5, whereas the other dimensionless distances in the streamwise and spanwise directions verify the inequations $\Delta_1^+ < 120$ and $\Delta_2^+ < 210$ that are strongly less stringent than the recommendations for wall-resolved LES given by Piomelli and Chasnov [55]. These results show clearly that the present grid is very coarse in the streamwise and spanwise directions. As a consequence, this PITM simulation does not require extremely large memory and computing time resources. For the simulation performed by Fröhlich *et al.* [53], and Breuer *et al.* [54], these dimensionless distances, Δ_1^+ and Δ_2^+, are below than 50 and 30, and 20 and 9, respectively.

5.3 Streamlimes and velocity vectors

Figure 6 shows the streamlines of the instantaneous flowfield in the mid-plane (x_1, x_3) of the channel at $x_2/h = 2$ for both PITM simulations. One can see clearly the presence of the zones of the flow recirculation that are more or less extended in the lower wall region. It is found that the large turbulent eddies simulated on the coarse grid are relatively week and smoothly varying. However, figure 21 will show that they are present and they correspond to an appreciable part of the fluctuating energy (see figure 19a). For each case, the flow separates in upstream locations of the hill crest and reattaches in downstream locations. The separation caused by the adverse pressure gradient results from the strong streamwise curvature of the lower wall. These snapshots of the instantaneous flowfield clearly illustrate the three dimensional nature of the flow although the geometry is two-dimensional. Figure 7 shows the streamlines plot of the averaged flowfield for both PITM simulations. One can see that the flow statistically separates at $x_1/h \approx 0.23$ downstream the hill crest and reattaches at $x_1/h \approx 4.3$. When comparing with figure 8 showing the streamlines of the flowfield computed by the RANS/RSM model [5], it appears that the RSM model predicts a too small recirculation zone that extends roughly from $x_1/h \approx 0.2$ to the approximate value 2.80. The reason of these different predictions is not clearly established, but one can reasonably invoke the instantaneous large eddies naturally issued from the streamwise curvature of the lower wall that play a major role in this type of flow. Figure 9 shows the snapshot of the vector plots of the instantaneous flow in the mid-plane $x_2/h = 2$. The unsteady character of the flow, well illustrated through the irregularity of the vector plots, is more pronounced in the recirculation zone and in the reattachment region.

5.4 Friction coefficient

Figure 10 displays the distribution of the friction coefficient $C_f = \tau_w/(0.5\rho U_b^2)$ along the lower wall for both simulations. Comparisons are made with the reference data [54], (note that figure 11(a) of reference [54] uses the definition $C_f = \tau_w/(\rho U_b^2)$). As a result of interest, one can see that both PITM simulations performed on the coarse and medium grids predict rather well the friction coefficient along the lower wall in good agreement with the reference data, even if it is overpredicted in the windward region of the first hill and slightly behind the second hill. The friction coefficient performed on the coarse and medium grids present almost similar evolutions, except in the leeward region of the first hill where a better agreement with the reference data is obtained for the PITM2 simulation. For both PITM simulations, the friction coefficient decreases behind the hill crest reaching a first minimum value at $x_1/h = 0.3$. Then, this coefficient slightly increases and diminishes again attaining a second-minimum value at approximately 2.77 that corresponds roughly to the location of the maximum reverse flow. Afterwards, the friction coefficient slowly reincreases towards the second hill crest passing through zero at the reattachment point at $x_1/h \approx 4.3$. It slightly decreases near the second leeward hill face at $x_1/h \approx 0.7$ suggesting that the boundary layer is decelerated and finally, reaches its maximum value shortly before the hill crest where the flow strongly accelerates. On the other hand, it appears that the RSM model prediction highly deviates from the reference data. The reattachment point is anticipated at $x_1/h = 2.8$ confirming the observation on figure 8 that the recirculation length is too small. Moreover, the friction coefficient is highly over-predicted when moving from the reattachment point to the windward region of the second hill.

5.5 Mean velocity

Figure 11 displays the mean velocity profiles $\langle u_1 \rangle / U_b$ at six stations $x_1/h = 0.05, 0.5, 2, 4, 6$ and 8. The selected positions include the regions in the entrance of the channel $x_1/h = 0.05$, just upon separation $x_1/h = 0.5$, in the middle of the recirculation zone close to the leeward hill face $x_1/h = 2$, prior to the reattachment $x_1/h = 4$, the post-reattachment and flow recovery $x_1/h = 6$, and finally, the region of accelerating flow on the windward slope of the hill $x_1/h = 8$. At the position $x_1/h = 0.05$, the streamwise velocity features a near-wall peak due to the preceding flow acceleration along the windward of the hill. At the position $x_1/h = 2$, the velocity near the wall is negative showing that the boundary layer is detached. The maximum reverse flow occurs in this region. In the post reattachment region after $x_1/h = 4$, the flow consists of the boundary layer which develops from the reattachment point and the wake originates from the separated shear layer further upstream. At the position $x_1/h = 8$, the flow is strongly accelerated due to the presence of the second hill. For both PITM simulations, one can see that the subfilter stress model provides velocity profiles that exhibit good agreement with the reference data at almost each position. The mean velocity profiles provided by the PITM1 simulation however presents some slight discrepancies in the immediate vicinity of the lower wall at two stations, $x_1/h = 2$ where the reverse flow is quasi-maximum and at $x_1/h = 6$ after the reattachment point whereas the mean velocity profiles associated with the PITM2 simulation agree better with the reference data. These slight differences observed between the PITM1 velocities and the data are probably attributed to the grid size which is not sufficiently refined in the streamwise direction for accurately

describing the strongly varying mean velocity profiles. On the other hand, it is found that the RSM model yields velocity profiles that disagree with the reference data on several important aspects, particularly at the positions $x_1/h = 2$, 4, and 6. The intensity of the flow recirculation is predicted too high at the position $x_1/h = 2$. Furthermore, the flow reattaches too early at the lower wall at the station $x_1/h = 4$ indicating that the RSM model is not able to satisfactory reproduce the recovery process. At this location, the boundary layer thickness is strongly underpredicted by the RSM model. The origin of the discrepancies with the data is not clear unless to mention that this type of flow is essentially governed by unsteady mechanisms that cannot be correctly mimicked by RANS models, even if using sophisticated RSM models.

5.6 Turbulent stresses

The total stresses τ_{ij} are obtained as the sum of the mean subfilter and resolved parts as indicated in equation (5). Figure 12 shows the turbulent shear stress τ_{13}/U_b^2 profiles at different positions of the channel for both simulations. The shear stress profiles produced by the PITM simulations present a qualitative good agreement with the reference data although some discrepancies can be observed in the lower wall region. More precisely, the turbulent peak that occurs at the stations $x_1/h = 0.5$ in the boundary layer of the lower wall is not well captured by the PITM1 simulation performed on the coarse grid. As encouraging results, it is better reproduced by the PITM2 simulation performed on the medium grid. The maximum negative value of the shear stress $\tau_{13}/U_b^2 \approx -0.034$ for $x_3/h \approx 1$ at the station $x_1/h = 2$ is under-predicted by the PITM1 simulation although the velocity in this position agrees relatively well with the data. In other positions, from the reattachment point to the windward portion of the hill, the agreement with the reference data is better obtained. Regarding the RANS computation, one can see that the RSM model returns over-predicted stresses in almost each position of the channel. The shear stress highly disagrees with the data in the windward regions of the first and second hill crests at $x_1/h = 0.05$ and $x_1/h = 8$, respectively. Figure 13 describes the turbulent energy k/U_b^2 profiles at different locations of the channel for both simulations. Like for the shear stress, a first observation reveals that the subfilter model returns a turbulent energy that agree well with the reference data. But the PITM1 simulation is not able to well captured the turbulent peaks at the two stations $x_1/h = 0.05$ and $x_1/h = 0.5$ that occur in the boundary layer of the lower wall because of the coarse grid resolution. Moreover, the turbulent energy is underpredicted in the region of the reverse flow at $x_1/h = 2$. As previously observed for the shear stress, the PITM2 performed on the medium grid provides better results than the PITM1 simulation performed on the coarse grid. The PITM2 simulation allows to accurately capture the turbulent peaks in the near wall region. Concerning the RANS computation, the RSM model returns turbulent energies that are slightly over-predicted at almost all the positions except at $x_1/h = 2$ and $x_1/h = 4$ where the turbulent energy is on the contrary under-predicted in the core flow. Figures 14, 15, and 16 show the profiles of the streamwise, spanwise and normal turbulent stresses τ_{11}/U_b^2, τ_{22}/U_b^2 and τ_{33}/U_b^2, respectively, plotted at different locations for both simulations. For this type of flow, there is no doubt that the mean velocity is not only governed by the turbulent shear stress, but also by the normal stresses which play an important role in the determining of the flow structures due to the streamline curvature. A first sight reveals that the subfilter model returns turbulent stresses in relatively good agreement with the reference data

for almost all positions. However, as it was already noticed in figure 13 for the turbulent energy, the turbulent peaks appearing in the boundary layer for the streamwise stresses τ_{11} and normal stresses τ_{22} at the two stations $x_1/h = 0.05$ and $x_1/h = 0.5$ are not very well captured by the PITM1 simulation performed on the coarse grid whereas they are better predicted by the PITM2 simulation performed on the medium grid. For both PITM simulations, the turbulent peaks of the spanwise and normal stresses, τ_{22} and τ_{33} are of lower intensity in the upper wall region. As it could be expected, it is finally found that the PITM2 simulation performed on the medium grid provides better results than the PITM1 simulation performed on the coarse grid. One can explain this outcome thanks to the grid refinement in the streamwise and spanwise directions that allows a better resolution of the flow. In particular, the three-dimensional component in the spanwise direction plays an essential role in the vortex stretching mechanisms of the flow and therefore in the prediction of the turbulence intensity. The RSM model provides turbulent stresses with an almost satisfactory overall turbulence level but the shape of the individual profiles is not well recovered. For both simulations, it can be noted that the flow anisotropy is well reproduced thanks to the pressure-strain correlation term that redistributes the energy among the different stress components. This term appearing only in second-moment closures demonstrates the usefulness of the present sufbilter stress model providing a more realistic flow prediction than viscosity based subgrid scale models. The study of the turbulent stresses provides a clue for analyzing the mean flow because of the coupling that exists between the mean motion equation and the turbulent transport equations. Figures 12 to 16 have shown that the RSM model returned overpredicted turbulent stresses. As a consequence, the mean flow produced by the RSM model is too much dissipated leading to a reduction of the recirculation length.

5.7 Sharing out of the turbulent energy

As shown in preceding sections, the subfilter stress model is mainly governed by the function $c_{sfs\epsilon_2}(\eta_c)$ that acts like a dynamical parameter which controls the spectral distribution. So that it is worth analyzing the sharing out of the turbulent energy among the subfilter and resolved turbulence scales. The first step consists of plotting the evolution of the coefficient $c_{sfs\epsilon_2}$ versus the wall distance. Different positions at $x_1/h = 0.5, 4, 6$ have been selected. As shown by figure 17, the subfilter coefficient $c_{sfs\epsilon_2}$ varies in the range [1.6,1.9]. These values stay nicely in scale between the two extreme RANS limiting values $c_{\epsilon 1} = 1.45$ and $c_{\epsilon 2} = 1.90$ according to equation (19). One can see that the function $c_{sfs\epsilon_2}$ goes to the RANS limit $c_{\epsilon 2} = 1.90$ very near the walls and decreases when moving to the centerline of the channel. This results means that the subfilter stress model behaves more or less like the RANS/RSM model in the near wall region, although the grid is very refined in the normal direction, and like LES in the core flow. Figure 18 illustrates the sharing out of the turbulent energy in the flow at the same positions $x_1/h = 0.5$, 4 and 6. As expected, one can see that the subfilter energy is of higher intensity than the resolved energy in the near wall region whereas the reverse situation occurs in the center of the channel. As a result of interest, it appears that the subfilter energy is very large in the near wall region even for a large cutoff wave number. When computing the total energy as the sum of the subfilter and resolved energies, one can observe a qualitatively good agreement with the reference data [54]. Figures 19 (a) and (b) show the contours of the ratio of the subfilter energy to the molecular

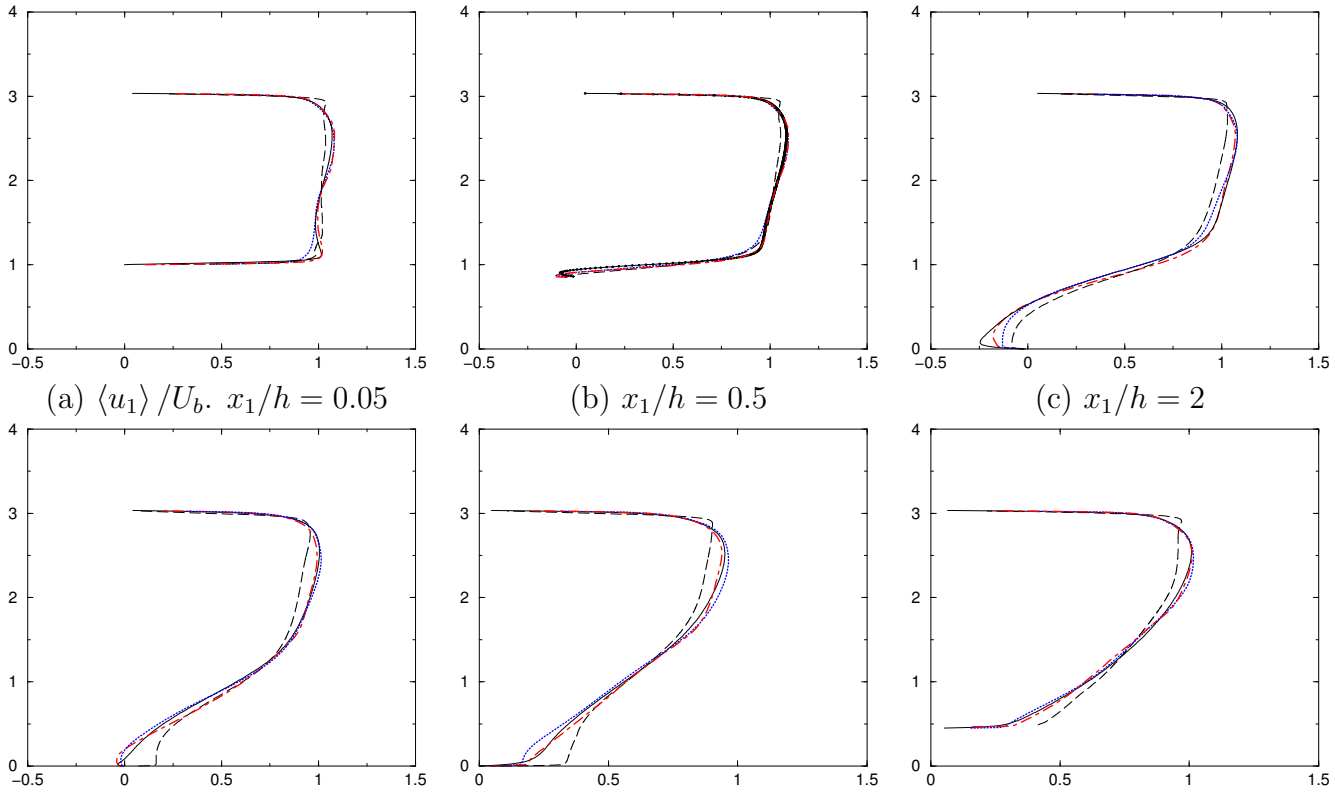

(a) $\langle u_1 \rangle / U_b$. $x_1/h = 0.05$ (b) $x_1/h = 0.5$ (c) $x_1/h = 2$

(d) $x_1/h = 4$ (e) $x_1/h = 6$ (f) $x_1/h = 8$

Figure 11. Streamwise velocity $\langle u_1 \rangle / U_b$ at different locations ($x_1/h = 0.05$, 0.5, 2, 4, 6, 8. LES (Breuer *et al.*, 2009) —; PITM1 ($80 \times 30 \times 100$ ···; PITM2 ($160 \times 60 \times 100$) -.-.; RSM - -

viscosity $\mu_{sfs}/\mu = (c_\mu \rho k_{sfs}^2/\epsilon)/\mu$ as well as the ratio of the total energy to the molecular viscosity $\mu_t/\mu = (c_\mu \rho k^2/\epsilon)/\mu$, respectively, in the mid-plane $x_2/h = 2$ for the PITM simulation performed on the coarse grid $80 \times 30 \times 100$. The ratio of the subfilter energy to the molecular viscosity ranges from zero to the approximate value 150 indicating an appreciable subfilter viscosity contribution given by the turbulence model. Obviously, this result is dependent on the grid resolution. Figure 19 (a) reveals that the distribution of the subfilter viscosity is more pronounced in the second leeward hill region than in the first hill region, suggesting a strong turbulence activity. Owing to the fact that the ratio μ_t/μ is related to the ratio μ_{sfs}/μ by the relation $\mu_t/\mu = (k/k_{sfs})^2 \mu_{sfs}/\mu$, one can see from figure 19 (b) that the ratio of the total viscosity to the molecular viscosity reaches the maximum value 900. The total turbulence viscosity is of higher intensity in the core flow region behind the second hill. The differences observed between the viscosity contours plotted in figure 19 (a) and 19 (b) are attributed to the resolved turbulence energy contribution which is of higher intensity in the core flow than in the boundary layers.

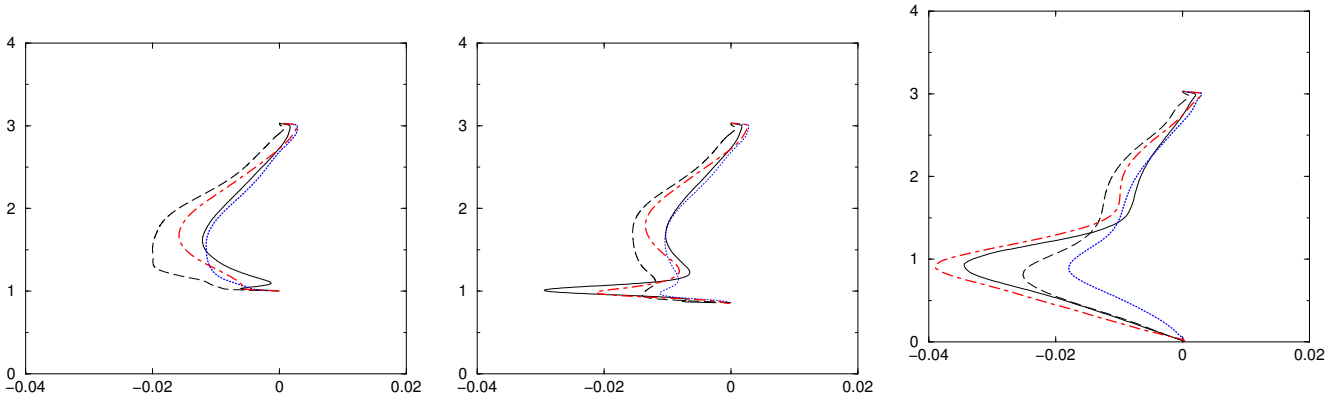

(a) τ_{13}/U_b^2. $x_1/h = 0.05$ (b) $x_1/h = 0.5$ (c) $x_1/h = 2$

(d) $x_1/h = 4$ (e) $x_1/h = 6$ (f) $x_1/h = 8$

Figure 12. Turbulent shear stress τ_{13}/U_b^2 at different locations ($x_1/h = 0.05$, 0.5, 2, 4, 6, 8. LES (Breuer *et al.*, 2009) —; PITM1 ($80 \times 30 \times 100$) $\cdots$; PITM2 ($160 \times 60 \times 100$) -.-.; RSM - -

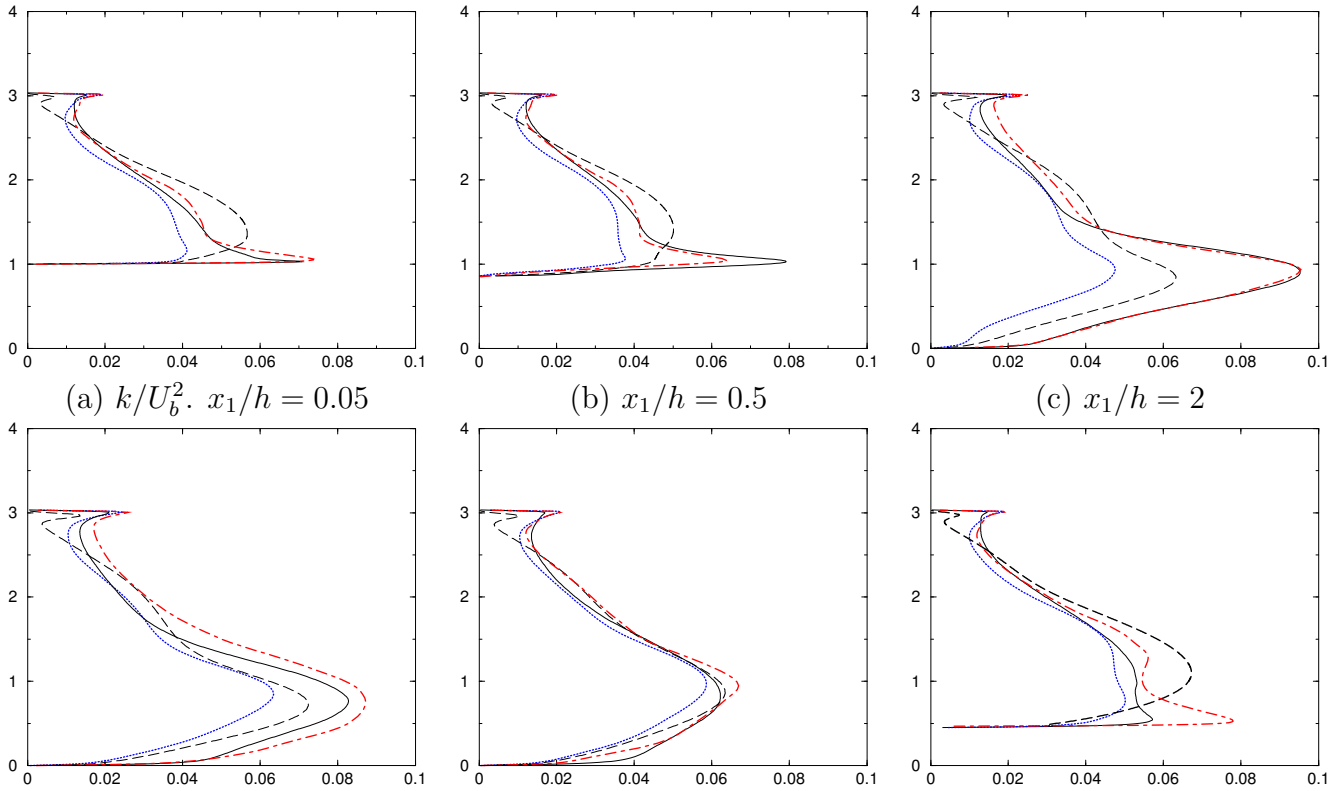

(a) k/U_b^2. $x_1/h = 0.05$ (b) $x_1/h = 0.5$ (c) $x_1/h = 2$

(d) $x_1/h = 4$ (e) $x_1/h = 6$ (f) $x_1/h = 8$

Figure 13. Turbulent energy k/U_b^2 at different locations ($x_1/h = 0.05$, 0.5, 2, 4, 6, 8) LES (Breuer *et al.*, 2009) —; PITM1 ($80 \times 30 \times 100$) $\cdots$; PITM2 ($160 \times 60 \times 100$) -.-.; RSM - -

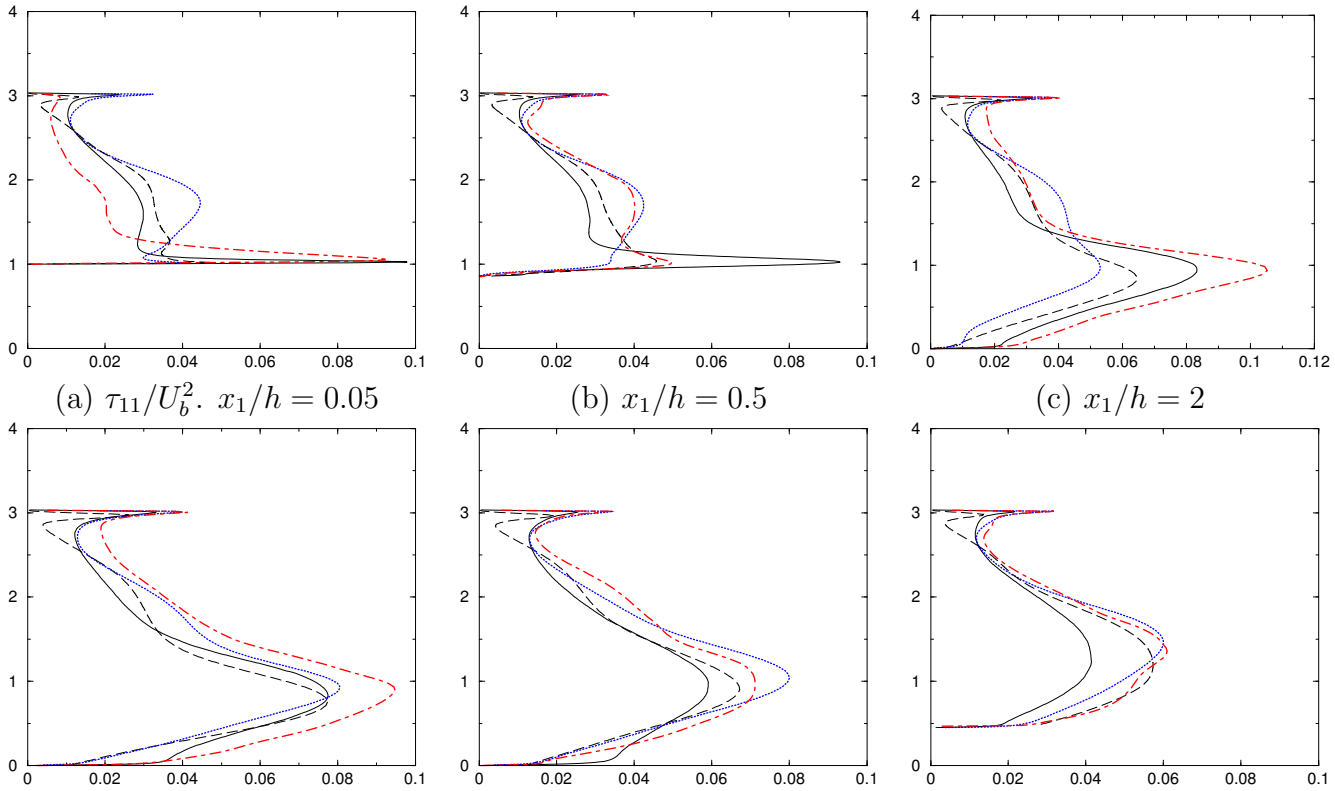

(a) τ_{11}/U_b^2. $x_1/h = 0.05$ (b) $x_1/h = 0.5$ (c) $x_1/h = 2$

(d) $x_1/h = 4$ (e) $x_1/h = 6$ (f) $x_1/h = 8$

Figure 14. Streamwise turbulent energy τ_{11}/U_b^2 at different locations ($x_1/h = 0.05$, 0.5, 2, 4, 6, 8) LES (Breuer *et al.*, 2009) —; PITM1 ($80 \times 30 \times 100$) $\cdots$; PITM2 ($160 \times 60 \times 100$) -.-.; RSM - -

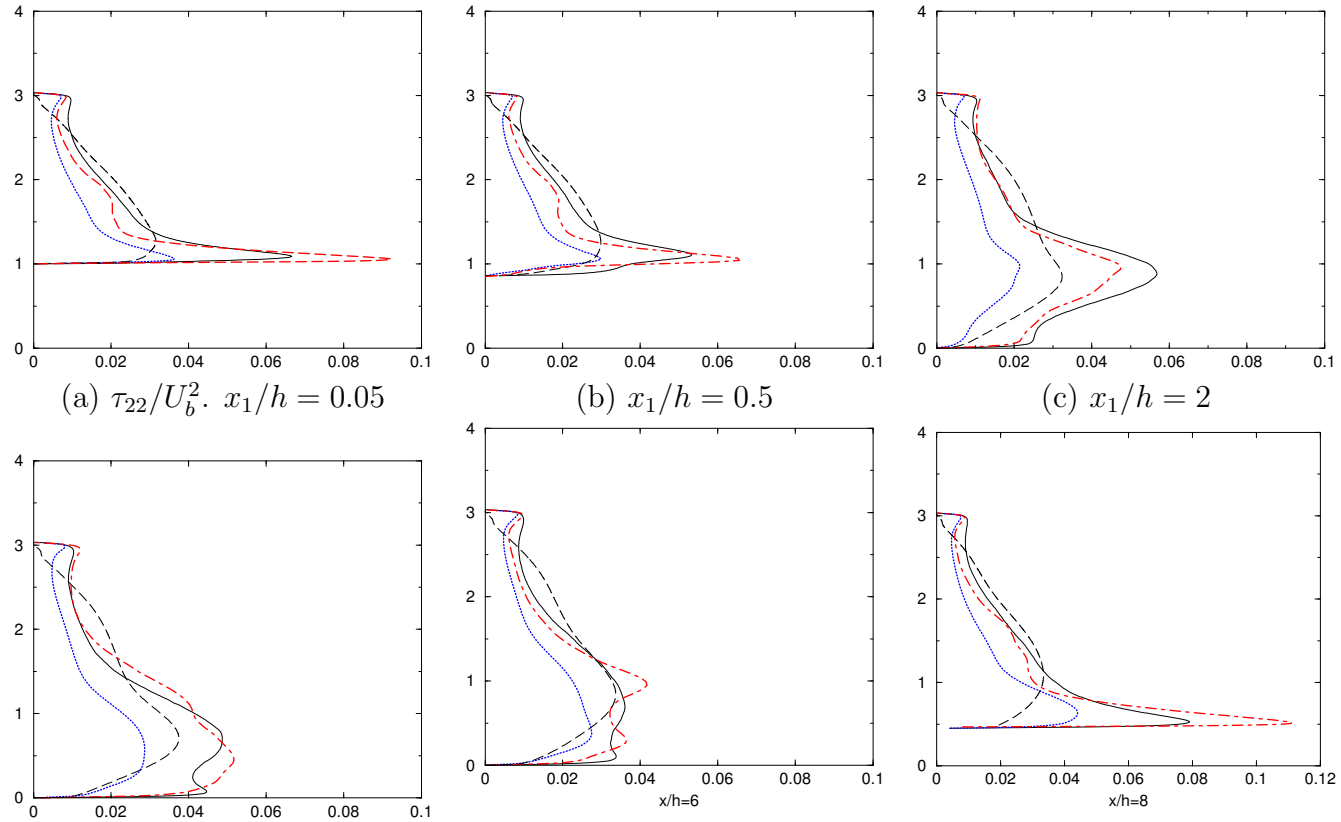

(a) τ_{22}/U_b^2. $x_1/h = 0.05$ (b) $x_1/h = 0.5$ (c) $x_1/h = 2$

(d) $x_1/h = 4$ (e) $x_1/h = 6$ (f) $x_1/h = 8$

Figure 15. Spanwise turbulent energy τ_{22}/U_b^2 at different locations ($x_1/h = 0.05$, 0.5, 2, 4, 6, 8) LES (Breuer *et al.*, 2009) —; PITM1 ($80 \times 30 \times 100$) $\cdots$; PITM2 ($160 \times 60 \times 100$) -.-.; RSM - -

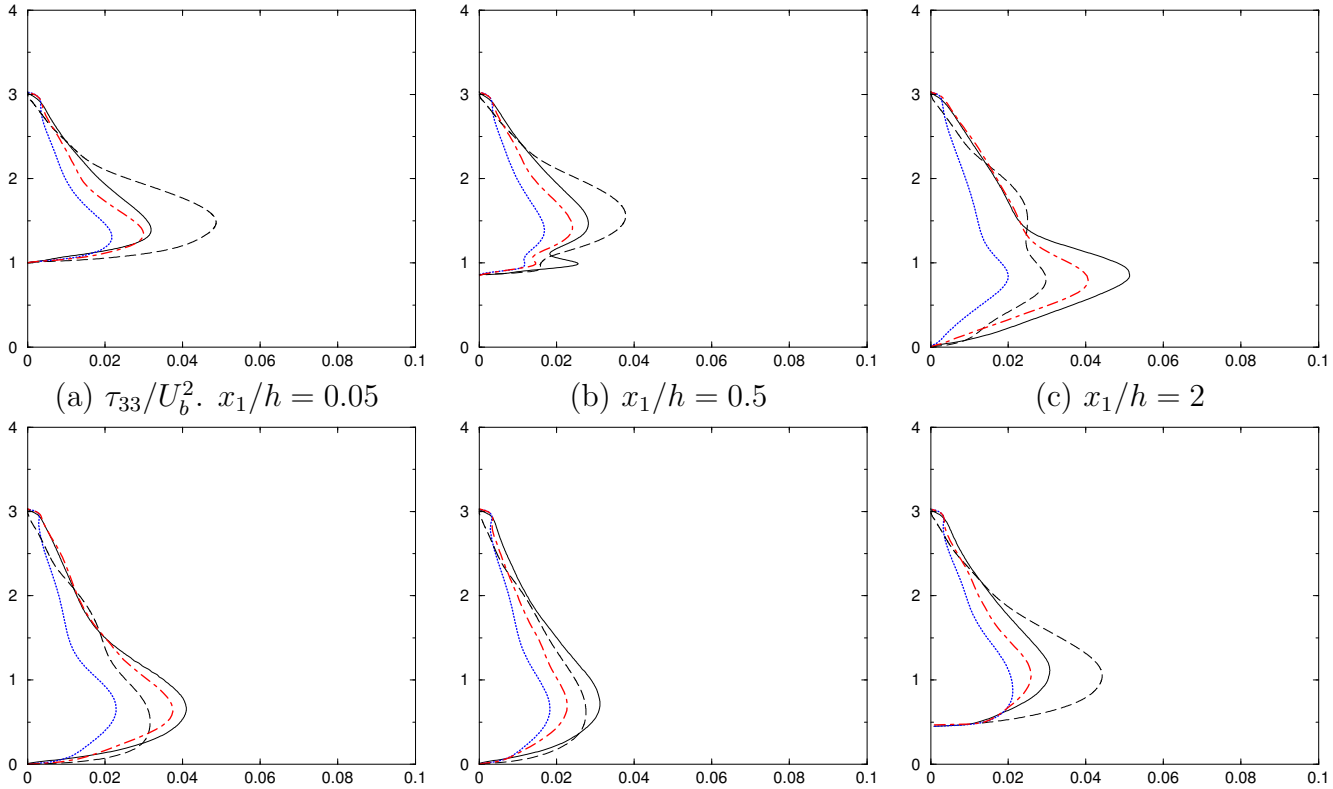

(a) τ_{33}/U_b^2. $x_1/h = 0.05$ (b) $x_1/h = 0.5$ (c) $x_1/h = 2$

(d) $x_1/h = 4$ (e) $x_1/h = 6$ (f) $x_1/h = 8$

Figure 16. Turbulent energy in the normal direction to the walls τ_{33}/U_b^2 at different locations ($x_1/h = 0.05$, 0.5, 2, 4, 6, 8) LES (Breuer *et al.*, 2009) —; PITM1 ($80 \times 30 \times 100$) $\cdots$; PITM2 ($160 \times 60 \times 100$) -.-.; RSM - -

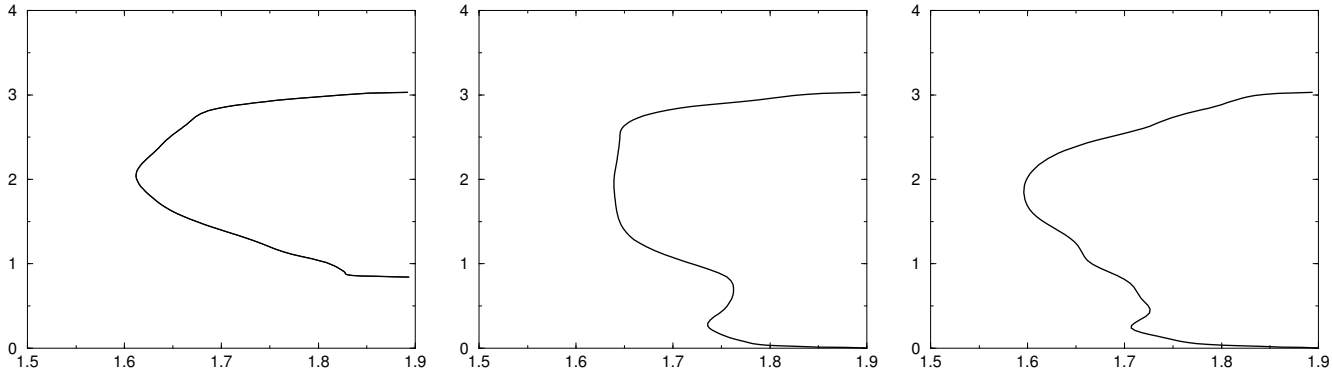

(a) $c_{sfs\epsilon_2}$. $x_1/h = 0.5$ (b) $x_1/h = 4$ (c) $x_1/h = 6$

Figure 17. Evolution of the subfilter-scale coefficient $c_{sfs\epsilon_2}$ defined in equation (19) at different locations $x_1/h = 0.5, 4, 6$. PITM1 ($80 \times 30 \times 100$)

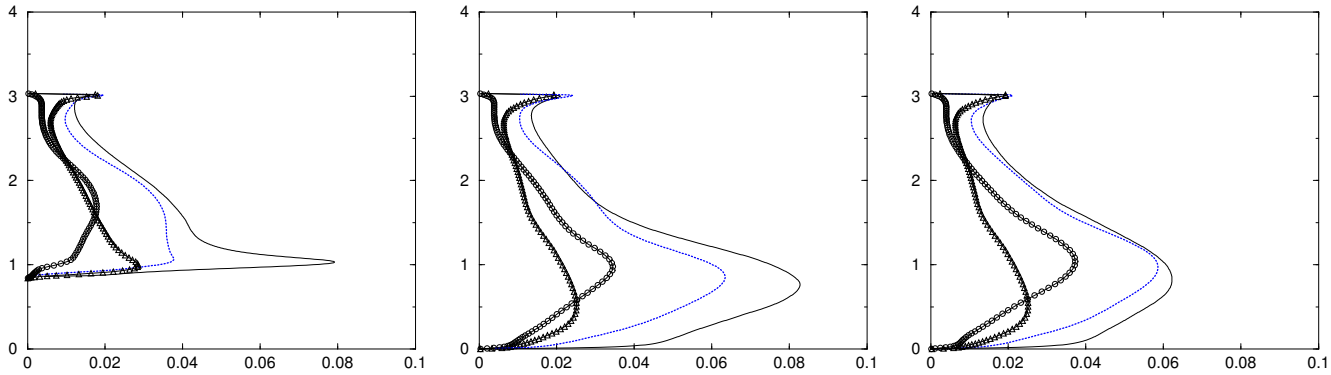

(a) k/U_b^2. $x_1/h = 0.5$ (b) $x_1/h = 4$ (c) $x_1/h = 6$

Figure 18. Sharing out of the turbulent energy k/U_b^2 at $x_1/h = 0.5, 4, 6$
LES (Breuer *et al.*, 2009) —; subfilter scale energy k_{sfs} Δ ; resolved scale energy k_{les} $\circ$;
total energy k $\cdots$ PITM1 ($80 \times 30 \times 100$)

5.8 Flow anisotropy

Figure 20 describes the solution trajectories along vertical lines starting from the lower wall towards the upper wall at different streamwise locations, that are projected onto the second and third invariant planes formed by the anisotropy tensor. In this framework, Lumley [56] has demonstrated that the possible states of turbulence must remain inside a curvilinear triangle delimited by the straight line of the two-dimensional state satisfying equation $A_3 - A_2 + 8/9 = 0$ and by two curves of axisymmetric states of equations $|A_2| = 6^{1/3}\, A_3^{2/3}$. For isotropic flows, the flatness parameter A goes to unity since the invariants A_2 and A_3 are zero whereas near the walls, A is close to zero because of the two component limit turbulence states. Each diagram of figure 20 shows that the solution trajectories stay inside the curvilinear triangle of realizability, confirming that the realizability conditions [57] which imply non-negative values of the three principal invariants I_i, appearing in the characteristic polynomial $P(\lambda) = \lambda^3 - I_1\lambda^2 + I_2\lambda - I_3$ deduced from the eigenvalue equation $|\tau_{ij} - \lambda\delta_{ij}| = 0$, are perfectly satisfied.

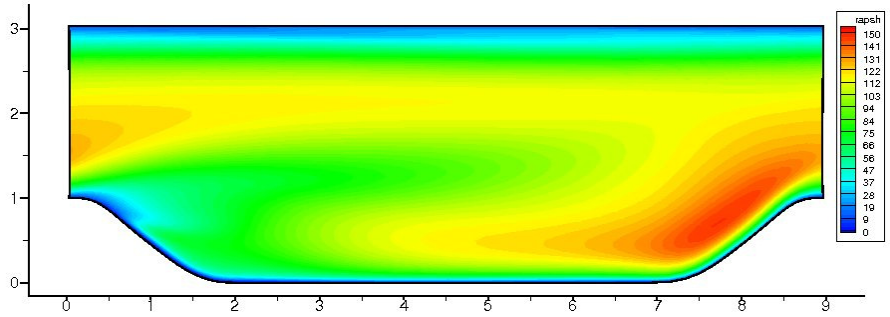

(a)

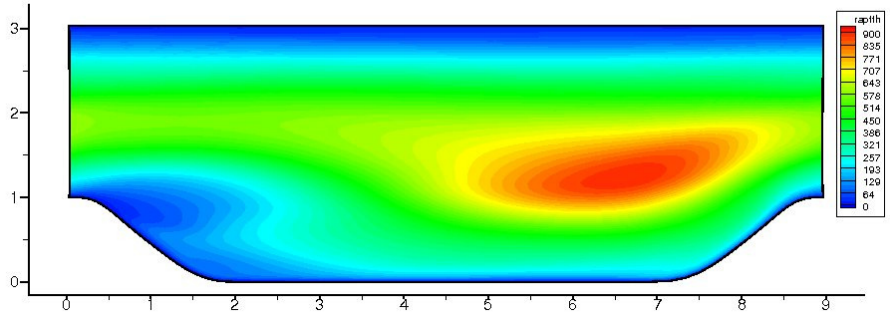

(b)

Figure 19. Contours of the ratio of subfilter/total energy to molecular viscosity in the mid-plane at $x_2/h = 2$. (a) $\mu_{sfs}/\mu = (c_\mu \rho k_{sfs}^2/\epsilon)/\mu$; (b) $\mu_t/\mu = (c_\mu \rho k^2/\epsilon)/\mu$. PITM1 ($80 \times 30 \times 100$)

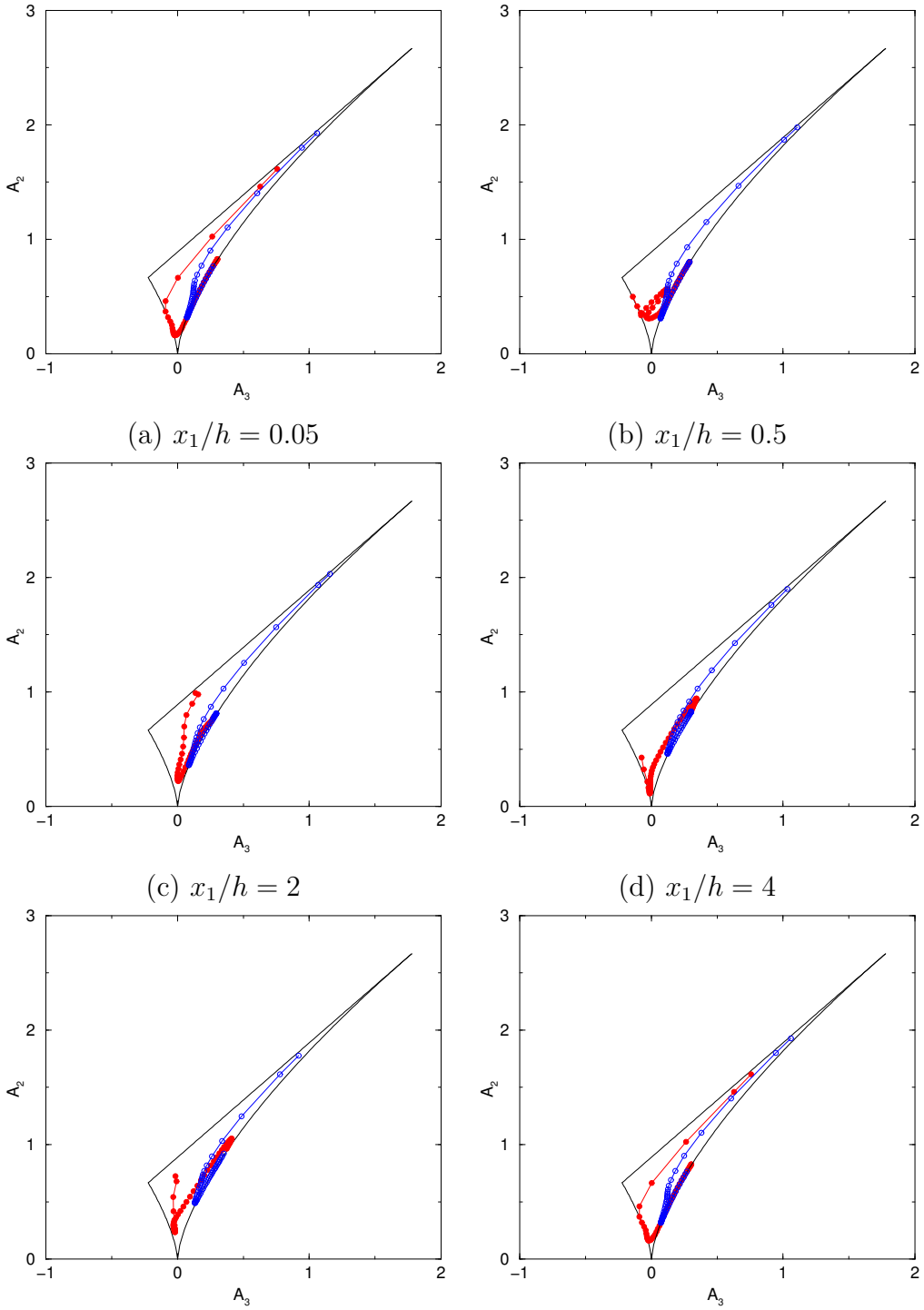

(a) $x_1/h = 0.05$ (b) $x_1/h = 0.5$

(c) $x_1/h = 2$ (d) $x_1/h = 4$

(e) $x_1/h = 6$ (f) $x_1/h = 8$

Figure 20. Solutions trajectories along vertical lines at different locations ($x_1/h = 0.05$, 0.5, 2, 4, 6, 8.) projected onto the second-invariant/third-invariant plane formed by the anisotropy tensor $a_{ij} = (\tau_{ij} - \frac{2}{3}k)/k$. • lower wall; ○ upper wall. PITM1 ($80 \times 30 \times 100$)

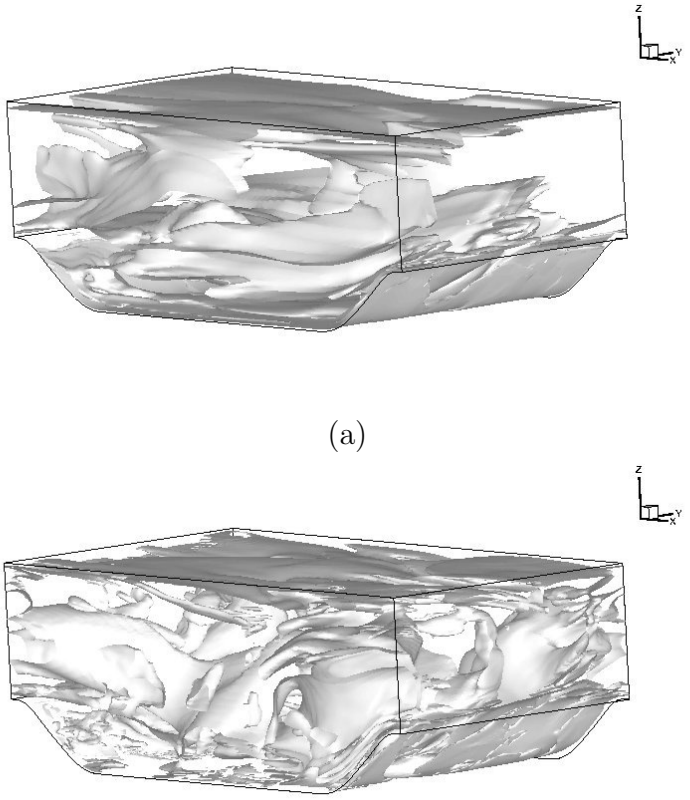

(a)

(b)

Figure 21. Isosurface of instantaneous filtered vorticity. $\omega = 200\ s^{-1}$. (a) PITM1 ($80 \times 30 \times 100$) ; (b) PITM2 ($160 \times 60 \times 100$)

Moreover, it is possible to see that the trajectories start from the straight line of two-component limit corresponding to the lower or the upper wall and finally get back again to the linear side of the realizability triangle. It can be remarked also that the flow anisotropy is more pronounced near the upper wall than near the lower wall. Then, the trajectories are passing near the origin of the diagram that represents a more isotropic state. Indeed, this position roughly corresponds to the centered region of the channel where the stresses are more isotropic, as also observed in Figures 14, 15 and 16. These predictive elements are found to be in qualitative agreement with the previous analysis of the invariant map conducted by Fröhlich *et al.* [53] and Breuer *et al.* [54].

5.9 Flow structures

Figures 21 (a), (b) show the isosurfaces of instantaneous vorticity modulus for the PITM flow simulations performed on the coarse and medium grids, respectively. These figures reveal the

presence of elongated vortices that develop in the entire channel and clearly demonstrates the three dimensional nature of the flows. Due to the flow recirculation, a strong turbulence activity is visible near the lower wall. One can remark that both PITM simulations succeed in reproducing qualitatively these dynamical structures. But the PITM2 simulation performed on the medium grid $160 \times 60 \times 100$ is able to capture large scales and also smaller scales due to the grid refinement effects, as it could be seen when comparing figure 21(a) and 21(b). Therefore, figure 21(b) shows a more realistic description of the flow structures than figure 21(a), even if the grid resolution is not really sufficient in the streamwise and spanwise directions to get a fine definition of the structures. In that sense, a more quantitative structural information requires DNS or highly resolved LES grid resolutions to be properly computed. Obviously, the RSM computation can only provide mean organized structures because of the RANS assumptions.

6 Conclusion

The subfilter stress model derived from the PITM method has been successfully used for simulating PITM continuous hybrid non-zonal RANS/LES internal flows. In a first step, the model has been validated against the well known fully turbulent channel flow. Then, it has been applied for simulating the separated flow in a channel with streamwise periodic constrictions. With regard to highly resolved LES requiring refined grids, the present simulations have been performed on a very coarse grid and on a medium grid. As a result, it has been found that the subfilter stress model simulates fairly well this flow with complex physics involving turbulence mechanisms associated with separation, recirculation, reattachment, acceleration and wall effects. The mean velocity and turbulent stresses agree fairly well with the reference data but slight discrepancies are however observed in the immediate vicinity of the lower wall, mainly for the PITM1 simulation performed on the very coarse grid. As expected, the PITM2 simulation performed on the medium grid is more accurate than the PITM1 performed on the coarse grid because of the grid refinement. In contrast with the subfilter model, the RSM model inaccurately predicts this flow, essentially because the recirculation length is under-estimated. As a consequence, the RSM velocities present some discrepancies with the reference data in the lower wall region. But it appears that the RSM stress levels are relatively well predicted although slightly over-predicted in comparison with the reference data. This failure seems attributed to the inability of RANS models to capture the large-scale dynamics in the separated shear layer which play a pivotal role in the turbulent mechanisms. Finally, this work shows that the present subfilter stress model seems to be a good candidate for simulating engineering turbulent flows with complex physics, with a drastic saving of computational cost, provided however that the numerical scheme is sufficiently stable and precise for accurately capturing the unsteady large scales of the flow.

References

[1] R. Schiestel. *Modeling and simulation of turbulent flows.* ISTE Ltd and J. Wiley, 2008.

[2] B. E. Launder and N. Shima. Second moment closure for the near wall sublayer: Development and application. *AIAA Journal*, 27(10):1319–1325, 1989.

[3] B. Chaouat. Numerical predictions of channel flows with fluid injection using a Reynolds stress model. *Journal of Propulsion and Power*, 18(2):295–303, 2002.

[4] K. Hanjalic and S. Jakirlic. Contribution towards the second-moment closure modeling of separating turbulent flows. *Computers and Fluids*, 27(2):137–156, 1998.

[5] B. Chaouat. Reynolds stress transport modeling for high-lift airfoil flows. *AIAA Journal*, 44(10):2390–2403, 2006.

[6] T. B. Gatski, C. L. Rumsey, and R. Manceau. Current trends in modelling research for turbulent aerodynamic flows. *Phil. Trans. Royal Society*, 365:2389–2418, 2007.

[7] M. Germano. A statistical formulation of the dynamic model. *Physics of Fluids*, 8(2):565–570, 1996.

[8] M. Lesieur and O. Metais. New trends in large-eddy simulations of turbulence. *Ann. Rev Journal of Fluid Mechanics*, 28:45–82, 1996.

[9] B. Chaouat and R. Schiestel. Reynolds stress transport modelling for steady and unsteady channel flows with wall injection. *Journal of Turbulence*, 3:1–15, 2002.

[10] J. Smagorinsky. General circulation experiments with the primitive equations. *Mon. Weather Rev.*, 91(3):99–164, 1963.

[11] R. Spalart P. Detached-eddy simulation. *Annual Reviews Fluid Mechanics*, 41:181–202, 2009.

[12] J. Fröhlich and D. Von Terzi. Hybrid LES/RANS methods for the simulation of turbulent flows. *Progress in Aerospace Sciences*, 44(5):349–377, 2008.

[13] S. Basara and S. Jakirlic. A new hybrid turbulence modelling strategy for industrial cfd. *International Journal for numerical methods in fluids*, 42:89–116, 2003.

[14] B. Jaffrézic and M. Breuer. Application of an explicit algebraic Reynolds stress model within a hybrid LES-RANS method. *Flow, Turbulence and Combustion*, 81:415–448, 2008.

[15] K. Hanjalic and S. Kenjeres. Some developments in turbulence modeling for wind and environmental engineering. *Journal of Wind Engineering and Industrial Aerodynamics*, 96:1537–1570, 2008.

[16] F. Hamba. A hybrid RANS/LES simulation of turbulent channel flow. *Theoretical Computational Fluid Dynamics*, 16:387–403, 2003.

[17] L. Temmerman, M. Hadziabdic, M. A. Leschziner, and K. Hanjalic. A hybrid two-layer URANS-LES approach for large eddy simulation at high Reynolds numbers. *International Journal of Heat and Fluid Flow*, 26:173–190, 2005.

[18] F. Tessicini and M. A. Leschziner. Large eddy simulation of three-dimensional flow around a hill-shaped obstruction with a zonal near-wall approximation. *International Journal of Heat and Fluid Flow*, 27:894–908, 2007.

[19] L. Davidson and M. Billson. Hybrid LES-RANS using synthesized turbulent fluctuations for forcing in the interface region. *International Journal of Heat and Fluid Flow*, 27:1028–1042, 2006.

[20] F. Mathey, D. Cokljat, J. P. Bertoglio, and E. Sergent. Assessment of the vortex method for large eddy simulation inlet conditions. *Progress in Computational Fluid Dynamics*, 6(1):58–67, 2006.

[21] G. De Prisco, U. Piomelli, and A. Keating. Improved turbulence generation techniques for hybrid RANS/LES calculations. *Journal of Turbulence*, 9(5):1–20, 2008.

[22] C. Fan, X. Xudong, J. R. Edwards, H. A Hassan, and R. A. Baurle. Hybrid large-eddy/Reynolds-averaged Navier-Stokes simulations of shock-separated flows. *Journal of Spacecraft and Rockets*, 41(6):897–906, 2004.

[23] P. R. Spalart. Strategies for turbulence modelling and simulations. *International Journal of Heat and Fluid Flow*, 21:252–263, 2000.

[24] P. R. Spalart, S. Deck, M. L. Shur, K. D. Squires, M. Kh. Strelets, and A. Travin. A new version of detached-eddy simulation, resistant to ambiguous grid densities. *Theoretical Computational Fluid Dynamics*, 20:181–195, 2006.

[25] C. G. Speziale. Turbulence modeling for time-dependent RANS and VLES: A review. *AIAA Journal*, 36(2):173–184, 1998.

[26] C. Delanghe, B. Merci, and E. Dick. Hybrid RANS/LES modelling with an approximate renormalization group: I. model development. *Journal of Turbulence*, 6(13):1–18, 2005.

[27] M. J. Giles. Turbulence renormalization group calculations using statistical mechanics methods. *Physics of Fluids*, 6:595–604, 1994.

[28] B. Chaouat and R. Schiestel. A new partially integrated transport model for subgrid-scale stresses and dissipation rate for turbulent developing flows. *Physics of Fluids*, 17(065106):1–19, 2005.

[29] R. Schiestel and A. Dejoan. Towards a new partially integrated transport model for coarse grid and unsteady turbulent flow simulations. *Theoretical Computational Fluid Dynamics*, 18:443–468, 2005.

[30] B. Chaouat and R. Schiestel. From single-scale turbulence models to multiple-scale and subgrid-scale models by Fourier transform. *Theoretical Computational Fluid Dynamics*, 21(3):201–229, 2007.

[31] S. Jakirlic, S. Saric, G. Kadavelil, E. Sirbubalo, B. Basara, and B. Chaouat. SGS modelling in LES of wall-bounded flows using transport RANS models: from a zonal to a seamless hybrid LES/RANS method. *Proceeding* 6^{nd} *Symposium on Turbulent Shear Flow Phenomena*, 3:1057–1062, 2009.

[32] B. Chaouat and R. Schiestel. Progress in subgrid-scale transport modelling for continuous hybrid non-zonal RANS/LES simulations. *International Journal of Heat and Fluid Flow*, 30:602–616, 2009.

[33] S. Jakirlic, R. Manceau, S. Saric, A. Fadai-Ghotbi, B. Kniesner, S. Carpy, G. Kadavelil, C. Friess, C. Tropea, and J. Borée. LES, zonal and seamless hybrid LES/RANS: Rationale and applications to free and wall-bounded flows involving separations and swirl. In *Numerical simulation of turbulent flows and noise generation*, volume 104, pages 253–282. Ed. C. Brun, D. Juve, M, Manhart and C. D. Munz by Springer, 2009.

[34] A. Fadai-Ghotbi, C. Friess, R. Manceau, T. B. Gatski, and J. Borée. Temporal filtering: A consistent formalism for seamless hybrid RANS-LES modeling in inhomogeneous turbulence. *International Journal of Heat and Fluid Flow*, 31:378–389, 2010.

[35] S. S. Girimaji, E. Jeong, and R. Srinivasan. Partially averaged Navier-Stokes method for turbulence: Fixed point analysis and comparisons with unsteady partially averaged Navier-Stokes. *Journal of Applied Mechanics, ASME*, 73(3):422–429, 2006.

[36] B. Chaouat and R. Schiestel. Further insight into subgrid-scale transport modeling for continuous hybrid RANS/LES flow simulations. *Proceeding* 6^{nd} *Symposium on Turbulent Shear Flow Phenomena*, 3:1063–1068, 2009.

[37] R. Schiestel and B. Chaouat. On partially integrated transport models for subgrid-scale modelling. *ERCOFTAC Bulletin*, 72:49–54, 2007.

[38] A. Fadai-Ghotbi, C. Friess, R. Manceau, T. Gatski, and J. Borée. Toward a consistent formalism for seamless hybrid RANS-LES modelling in inhomogeneous turbulence based on temporal filtering. *Proceeding* 6^{nd} *Symposium on Turbulent Shear Flow Phenomena*, 3:1051–1056, 2009.

[39] J. W. Deardorff. The use of subgrid transport equations in a three-dimensional model of atmospheric turbulence. *Journal of Fluid Engineering, ASME*, 95:429–438, 1973.

[40] M. M. Gibson and B. E. Launder. Ground effects on pressure fluctuations in the atmospheric boundary layer. *Journal of Fluid Mechanics*, 86:491–511, 1978.

[41] C. B. da Silva and J. C. F. Pereira. On the local equilibrium of the subgrid-scales: the velocity and scalar fields. *Physics of Fluids*, 108103:1–4, 2005.

[42] R. Schiestel. Multiple-time scale modeling of turbulent flows in one point closures. *Physics of Fluids*, 30(3):722–731, 1987.

[43] B. Chaouat. Simulations of channel flows with effects of spanwise rotation or wall injection using a Reynolds stress model. *Journal of Fluid Engineering, ASME*, 123:2–10, 2001.

[44] B. Chaouat. An efficient numerical method for RANS/LES turbulent simulations using subfilter scale stress transport equations. *International Journal for Numerical Methods in Fluids*, 67:1207–1233, 2011.

[45] G. Comte-Bellot and S. Corrsin. Simple Eulerian time correlation of full and narrow-band velocity signals in grid-generated, isotropic turbulence. *Journal of Fluid Mechanics*, 48:273–337, 1971.

[46] C. Cambon, D. Jeandel, and J. Mathieu. Spectral modelling of homogeneous non-isotropic turbulence. *Journal of Fluid Mechanics*, 104:247–262, 1981.

[47] R. Moser, D. Kim, and N. Mansour. Direct numerical simulation of turbulent channel flow up to $R_\tau = 590$. *Physics of Fluids*, 11(4):943–945, 1999.

[48] D. K. Lilly. Numerical simulations of developing and decaying two-dimensional turbulence. *Journal of Fluid Mechanics*, 45:395–415, 1971.

[49] R. Manceau, J. P. Bonnet, M. A. Leschziner, and F. Menter. 10th joint ERCOFTAC (SIG-15)/IAHR/QNET-CFD Workshop on refined flow modelling, Poitiers. Ed. by R. Manceau, J. P. Bonnet, M. A. Leschziner and F. Menter, LEA, CNRS/Université de Poitiers, France, 2002.

[50] L. Temmerman, M. A. Leschziner, C. P. Mellen, and J. Fröhlich. Investigation of wall-function approximation and subgrid-scale models in large eddy simulation of separated flow in a channel with streamwise periodic constrictions. *International Journal of Heat and Fluid Flow*, 24:157–180, 2003.

[51] S. Saric, S. Jakirlic, M. Breuer, B. Jaffrezic, G. Deng, O. Chikhaoui, J. Fröhlich, D. Von Terzi, M. Manhart, and N. Peller. Evaluation of detached-eddy simulations for predicting the flow over periodic hills. In *ESAIM Proceedings CEMRACS 2005; Computational aeroacoustics and computational fluid dynamics in turbulent flows*, volume 16, pages 133–145. Ed. by E. Cancès, J. F. Gerbeau, 2007.

[52] M. Breuer, B. Jaffrézic, and K. Arora. Hybrid LES-RANS techniques based on a one-equation near-wall model. *Theoretical Computational Fluid Dynamics*, 22:157–187, 2009.

[53] J. Fröhlich, C. Mellen, W. Rodi, L. Temmerman, and M. Leschziner. Highly resolved large-eddy simulation of separated flow in a channel with streamwise periodic constriction. *Journal of Fluid Mechanics*, 526:19–66, 2005.

[54] M. Breuer, N. Peller, Ch. Rapp, and M. Manhart. Flow over periodic hills. Numerical and experimental study in a wide range of Reynolds numbers. *Computers and Fluids*, 38:433–457, 2009.

[55] U. Piomelli and J. R. Chasnov. Large eddy simulations: theory and applications. In *Turbulence and Transition Modelling*, pages 269–331. Ed. by M. Hallback, D. S. Henningson, A. V. Johansson and P. H. Alfredson, Kluwer, 1996.

[56] J. L. Lumley. Computational modeling of turbulent flows. *Advances in Applied Mechanics*, 18:123–176, 1978.

[57] U. Schumann. Realizability of Reynolds stress turbulence models. *Physics of Fluids*, 20(5):721–725, 1977.